0830-L-02 NAS 1.29/3-2 97-07

NASA Tech Briefs

National Aeronautics and Space Administration

Electronic Components and Circuits

Electronic Systems

Physical Sciences

Materials

Computer Programs

Mechanics

Machinery

Fabrication Technology

Mathematics and Information Sciences

Life Sciences

1999-035333

97-07 July 1997

C

INTRODUCTION

Tech Briefs are short announcements of new technology derived from the research and development activities of the National Aeronautics and Space Administration. These Briefs emphasize information considered likely to be transferable across industrial, regional, or disciplinary lines and are issued to encourage commercial application.

Availability of NASA Tech Briefs and TSP's

Distribution of NASA Tech Briefs, a monthly periodical publication, is limited to engineers in U.S. Industry and to other domestic technology transfer agents. Requests for individual Tech Briefs or for Technical Support Packages (TSP's) announced herein should be addressed to

NASA Center for AeroSpace Information
Technology Transfer Office
800 Elkridge Landing Rd.
Linthicum Heights, MD 21090-2934
Telephone No. (301) 621-0245

Please reference the three-letter, five-digit control number located at the end of each Tech Brief. Information on NASA's Technology Utilization Program, its documents, and services is also available at the same facility.

Technology Utilization Officers and Patent Counsels are located at NASA field installations to provide technology-transfer access to industrial users. Inquiries can be made by writing to NASA field installations listed below.

Technology Utilization Officers and Patent Counsels

Ames Research Center
Technology Utilization Officer
Mail Code 223-3
Moffett Field, CA 94035

Patent Counsel
Mail Code 200-11
Moffett Field, CA 94035

Goddard Space Flight Center
Technology Utilization Officer
Mail Code 702-1
Greenbelt, MD 20771

Patent Counsel
Mail Code 204
Greenbelt, MD 20771

Lyndon B. Johnson Space Center
Technology Utilization Officer
Mail Code IC-4
Houston, TX 77058

Patent Counsel
Mail Code AL3
Houston, TX 77058

John F. Kennedy Space Center
Technology Utilization Officer
Mail Stop PT-PMO-A
Kennedy Space Center, FL 32899

Patent Counsel
Mail Code PT-PAT
Kennedy Space Center, FL 32899

Langley Research Center
Technology Utilization Officer
Mail Stop 143
Hampton, VA 23665

Patent Counsel
Mail Code 279
Hampton, VA 23665

Lewis Research Center
Technology Utilization Officer
Mail Stop 7-3
21000 Brookpark Road
Cleveland, OH 44135

Patent Counsel
Mail Code LE-LAW
21000 Brookpark Road
Cleveland, OH 44135

Jet Propulsion Laboratory
Technology Utilization Officer
Mail Stop 156-211
4800 Oak Grove Drive
Pasadena, CA 91109

NASA Resident Office-JPL
Technology Utilization Officer
Mail Stop 180-801
4800 Oak Grove Drive
Pasadena, CA 91109

Patent Counsel
Mail Code 180-801
4800 Oak Grove Drive
Pasadena, CA 91109

George C. Marshall Space Flight Center
Technology Utilization Officer
Code AT01
Marshall Space Flight Center,
AL 35812

Patent Counsel
Mail Code CC01
Marshall Space Flight Center,
AL 35812

John C. Stennis Space Center
Technology Utilization Officer
Code HA-30
Stennis Space Center, MS 39529

NASA Headquarters
Technology Utilization Officer
Code CU
Washington, DC 20546

Assistant General Counsel for Patent Matters
Code GP
Washington, DC 20546

Dryden Flight Research Center
Technology Utilization Officer
M/S D21-31
Bldg. 4832 Whse 7
Lilly Dr.
Edwards, CA 93523

NASA TechBriefs

National Aeronautics and Space Administration

July 1997
97-07

5 Electronic Components and Circuits

11 Electronic Systems

17 Physical Sciences

35 Materials

39 Computer Programs

43 Mechanics

51 Machinery

55 Fabrication Technology

61 Life Sciences

This document was prepared under the sponsorship of the National Aeronautics and Space Administration. Neither the United States Government nor any person acting on behalf of the United States Government assumes any liability resulting from the use of the information contained in this document, or warrants that such use will be free from privately owned rights.

4

BLANK PAGE

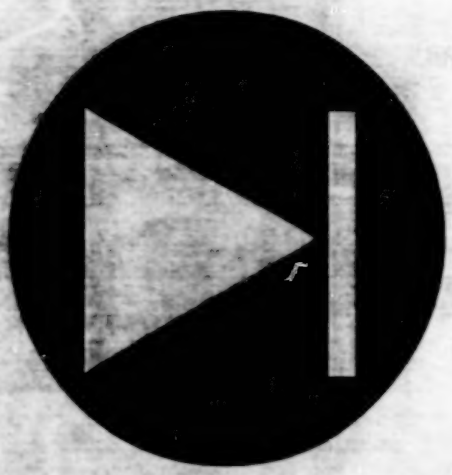

Electronic Components and Circuits

Hardware, Techniques, and Processes

7 Transverse-Mode Electron-Beam Microwave Generator

8 Wide-Band Operational-Amplifier Circuits

9 Active-Pixel Image Sensor With Regional Electronic Shutter

BLANK PAGE

Transverse-Mode Electron-Beam Microwave Generator

This device offers advantages over klystrons.

Goddard Space Flight Center, Greenbelt, Maryland

A vacuum-tube electron-beam device generates microwave energy via the interaction between an electron beam and an electromagnetic field in an evacuated cavity that has electrically conductive walls. In some respects, this device is similar to other vacuum-tube electron-beam microwave devices — especially klystrons — but it differs from klystrons in ways that offer significant advantages.

A klystron is said to operate in a longitudinal mode because its operation entails bunching of electrons along the beam, accompanied by interaction between the bunches of electrons and an electromagnetic field with an electric-field component parallel to the motion of electrons in the beam. To generate microwave power that can be extracted and used, it is necessary to amplify the electromagnetic field.

In a klystron, amplification depends on maintenance of the correct phase relationship between the motions of the bunched electrons and the electromagnetic field in the cavity. Thus, the operation of a klystron is sensitive to the times of flight of electrons and, therefore, to the voltages applied to accelerate the electron beam. The anti-bunching effect of the mutual repulsion of the electrons limits the achievable density of electrons and thus the available output power. Inasmuch as power losses caused by imperfections in cavity surfaces increase with frequency, the anti-bunching effect thus effectively limits the operating frequency; in practice, klystrons cannot generate useful amounts of power at frequencies above approximately 100 GHz.

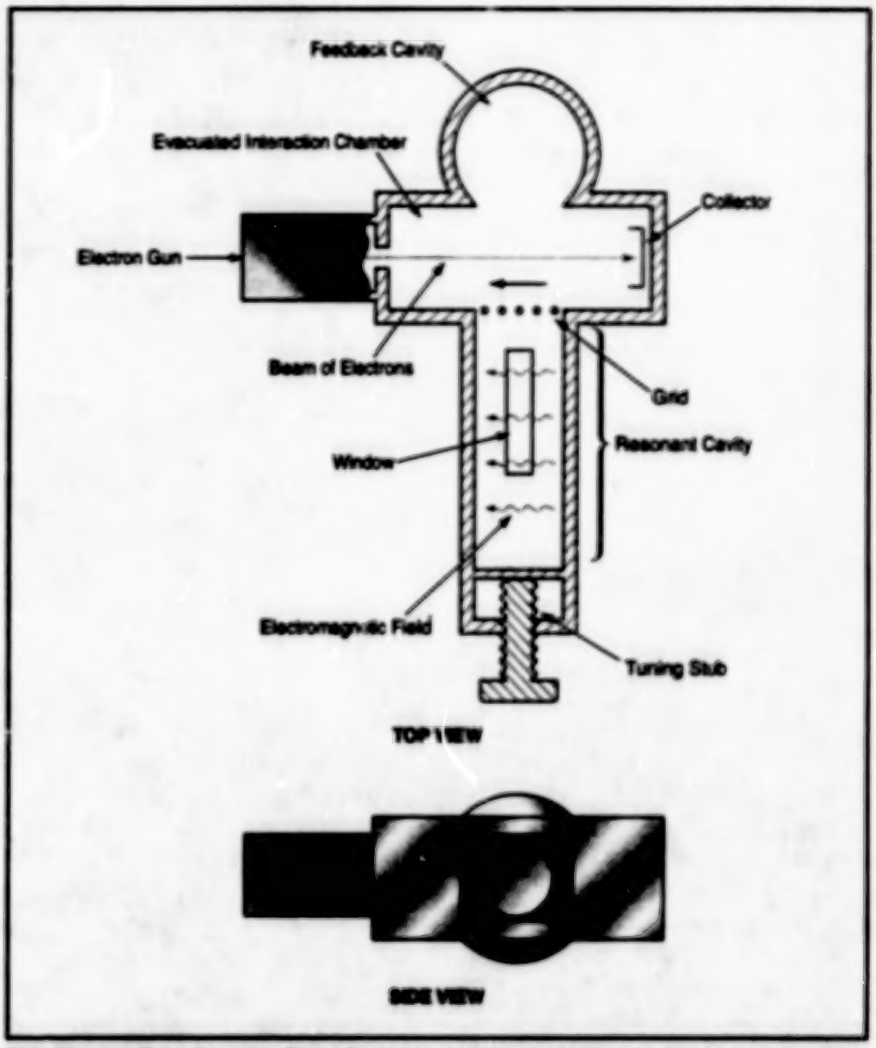

This Vacuum-Tube Electron-Beam Device is superior to a klystron in that its operation does not depend on maintenance of critical voltages, and it can generate a useful amount of power at higher frequency.

In the present device (see figure), an electron gun shoots a beam of electrons into an evacuated interaction chamber that has electrically conductive walls. After the electrons have traversed the interaction chamber and spent their energy interacting with the electromagnetic field in the chamber, they are collected by an electrode at a positive voltage at the end of the chamber opposite the electron gun.

At an opening in one of its side walls, the interaction chamber is joined to a rectangular resonant cavity that has conductive walls and a screw-adjustable conductive tuning stub. At an opening in the opposite side wall, the interaction chamber is connected to a conductive-walled spherical feedback cavity. The dimensions of the resonant cavity and the sphere are low-order multiples of the wavelength of operation. The frequency of operation is relatively insensitive to applied voltages; it is determined primarily by the dimensions of the resonant cavity and can be adjusted by moving the tuning stub.

A grid of wires spaced about half a wavelength apart is placed in the opening between the resonant cavity and the interaction chamber. The geometry of the feedback and resonant cavities, the grid, and the interaction chamber determines which electromagnetic-field modes can be sustained. Unlike a klystron, this device can be said to operate in transverse mode in the following sense: Electromagnetic waves propagate across the interaction chamber from the resonant cavity to the spherical feedback cavity, where they are transformed into waves that have radial electric-field components. These waves are reflected back into the interaction chamber, where they deflect the beam of electrons from side to side in an oscillating motion at the frequency of the electromagnetic field. The spatial variations of the electromagnetic field are such that as the beam oscillates sideways, it gives up energy to the field. Thus, the field becomes amplified. Electromagnetic energy is extracted for use through a window on one side of the resonant cavity.

Unlike a klystron, the present device does not depend on bunching. Consequently, its operating frequency is not limited by the anti-bunching effect. As a further consequence, it is not necessary to maintain a critical phase relationship between bunches of electrons and the electromagnetic field. Thus, the accelerating voltage in the electron gun can be

varied without adversely affecting the operation of the device; indeed, this voltage can be varied deliberately to modulate the microwave field.

This work was done by Lawrence Wharton of **Goddard Space Flight Center.** *Further information is contained in a TSP [see page 1].*

This invention is owned by NASA, and a patent application has been filed. Inquiries concerning nonexclusive or exclusive license for its commercial development should be addressed to the Patent Counsel, Goddard Space Flight Center [see page 1]. Refer to GSC-13521.

Wide-Band Operational-Amplifier Circuits

Frequency responses are extended by incorporation of suitably chosen input capacitances.

Goddard Space Flight Center, Greenbelt, Maryland

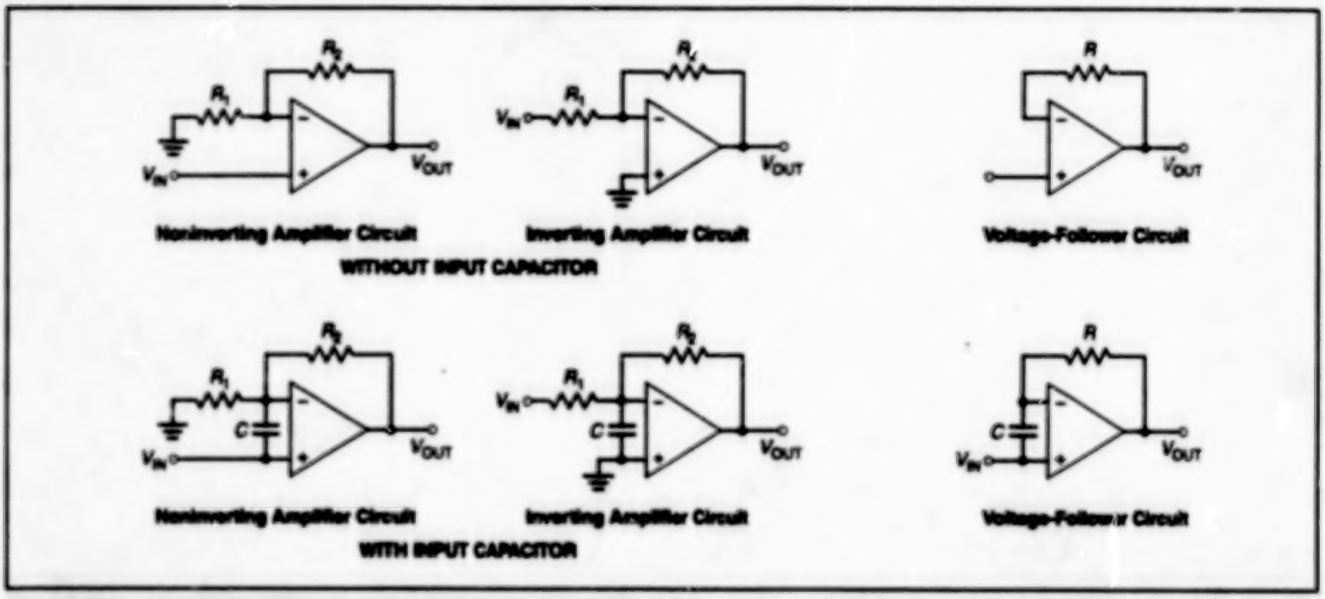

The Addition of Input Capacitors can extend the frequency responses of these circuits, provided that the values of capacitance are suitably chosen.

The top part of the figure illustrates typical operational-amplifier circuits with resistive feedback networks, while the bottom part of the figure illustrates circuits that are identical except for the connection of capacitors between the inverting (–) and noninverting (+) input terminals. The frequency response of each circuit can be extended by suitable choice of the capacitance, as explained below.

For each operational amplifier considered in isolation from other circuit components (the open-loop case), the magnitude of the gain (K) as a function of frequency (f) is given by

$$|K| = |K_0|/[1 + (f/f_3)^2]^{1/2},$$

where K_0 is the dc gain, and f_3 is a characteristic frequency popularly denoted the "3-dB rolloff frequency" because the power at that frequency is half (approximately 3 dB below) the power at zero frequency. When the operational amplifier is incorporated into a feedback circuit (the closed-loop case), the gain is altered by the presence of the other circuit components.

In the case of the inverting operational-amplifier circuit, the magnitude of the closed-loop gain is given by

$$|K_{FB}| = |V_{OUT}(f)/V_{IN}(f)| = (f_0/f)/[(1 + \alpha)^2 + |(f_0\alpha/f) - (f/f_0\alpha\beta)|^2]^{1/2},$$

where f_0 denotes the open-loop gain-bandwidth product $K_0 f_3$,

$$\beta = (R_1 + R_2)/(2\pi R_1 R_2 C \alpha f_0),$$

and α in this case equals R_1/R_2. For the noninverting operational-amplifier circuit, the corresponding equations are

$$|K_{FB}| = (f_0/f)/[1 + |(f_0\alpha/f) - (f/f_0\alpha\beta)|^2]^{1/2},$$

where α in this case equals

$$R_1/(R_1 + R_2).$$

For the voltage follower, the magnitude of the closed-loop gain is given by

$$|K_{FB}| = (f_0/f)/[1 + |(f_0/f) - (f/f_0\beta)|^2]^{1/2}$$

(for the voltage follower, $\alpha = 1$).

The following procedure can be used to select a suitable value of C for extending the frequency response of any of these circuits beyond that attainable without the capacitor:

1. Choose two different frequencies at which it is desired to have $|K_{FB}|$ equal a specified value. Let the specified value exceed the corresponding values of $|K_{FB}|$ at the chosen frequencies for the circuit without the input capacitor.
2. Using the chosen frequencies and the specified value of $|K_{FB}|$, find the value of β that satisfies the applicable one of the three equations for $|K_{FB}|$.
3. Once the value of β has been found, calculate C by use of

$$C = (R_1 + R_2)/(2\pi R_1 R_2 \alpha \beta f_0)$$

for the inverting or noninverting amplifier, or by use of $C = 1/2\pi R\beta f_0$ for the voltage follower.

This work was done by Leonard Kleinberg of **Goddard Space Flight Center.** *Further information is contained in a TSP [see page 1].*

This invention is owned by NASA, and a patent application has been filed. Inquiries concerning nonexclusive or exclusive license for its commercial development should be addressed to the Patent Counsel, Goddard Space Flight Center [see page 1]. Refer to GSC-13638.

Active-Pixel Image Sensor With Regional Electronic Shutter

Integration time in each region is adjusted to prevent saturation or loss of signal.

NASA's Jet Propulsion Laboratory, Pasadena, California

Scientific NASA applications — the star tracker, for instance — require imagers with wide dynamic ranges. When a single integration period for an entire image sensor is used (as in a CCD system) to capture bright stars with dim stars, either the bright star is properly exposed but the dim stars are lost in the noise, or the dim stars are properly exposed but the bright star is saturated. Ratios between brightnesses of objects captured in the same scene (e.g., a planet and nearby stars) might be as large as 10^8. To enable simultaneous observation of bright stars without saturation and dim stars without loss of signal, a sensor with regional-electronic-shutter capability is necessary. Such a sensor is described here.

In the star-tracker application, a spacecraft-guidance system determines spacecraft attitude by matching an observed star field to a star catalog. Typically, a few stars with different magnitudes are used for tracking in a given field of view. Using the regional electronic shutter, each star in the field of view can have its own integration period. This way, simultaneous capture of bright stars with dim stars is accommodated, enabling a large increase in tracker capability.

The regional electronic shutter provides a suitable integration time for each of several regions in different parts of the array. This is done by implementing individual pixel reset, which was previously reported in "Image Sensors With Individual Pixel Reset" (NPO-19735), *NASA Tech Briefs*, Vol. 20, No. 11, (November 1997), page 34, within each pixel thus controlling the integration time for a specific region. Individual pixel reset makes it possible to shorten integration time, such that if the illumination is high, the pixel still will not be saturated. This is done by controlling the reset gate via two lines that carry the column and row reset control voltages. When both the row- and column-address voltages are set high for the specific address, the pixel at that address can be reset. Using information from previous frames, the appropriate integration time for the region could be determined, and control is provided to implement this exposure time via a regional electronic shutter.

The concept has been implemented in a 64-by-64-pixel CMOS active pixel image sensor chip that achieves a dynamic range of 80 dB, a read noise of 50 electrons (root mean square), low dark current, and excellent electronic-shutter linearity. This prototype paves the way for lower-risk development of similar 1,024-by-1,024-pixel sensors with regional electronic-shutter capability.

This work was done by Orly Yadid-Pecht, Bedabrata Pain, Christopher Clark, Craig Staller, and Eric Fossum of Caltech for **NASA's Jet Propulsion Laboratory**. *Further information is contained in a TSP [see page 1].*

In accordance with Public Law 96-517, the contractor has elected to retain title to this invention. Inquiries concerning rights for its commercial use should be addressed to

Larry Gilbert, Director
Technology Transfer
California Institute of Technology
Mail Code 315 - 6
Pasadena, CA 91125
(818) 395-3288

Refer to NPO-19616, volume and number of this NASA Tech Briefs *issue, and the page number.*

BLANK PAGE

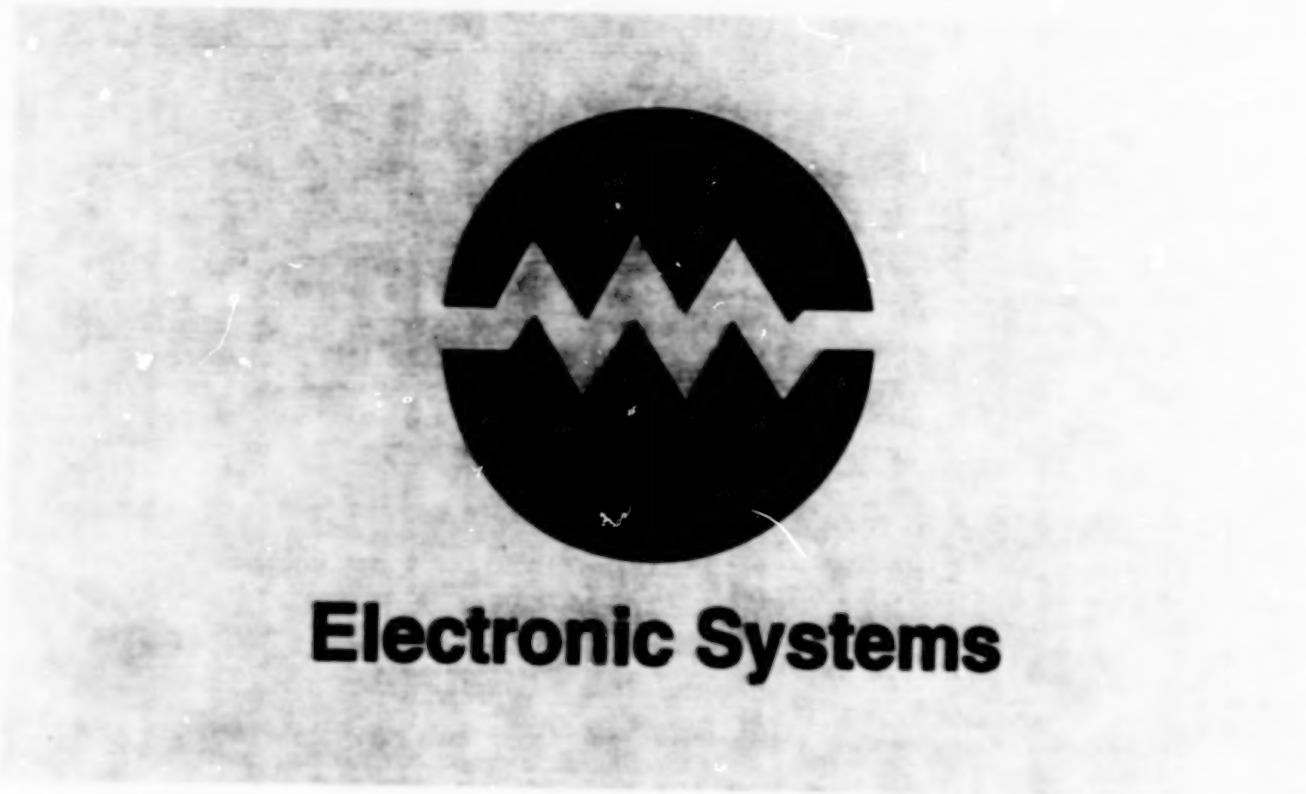

Electronic Systems

Hardware, Techniques, and Processes

13 Fast Three-Dimensional-Imaging Camera
14 Improved Ultraviolet-and-Infrared Hydrogen-Flame Detector
15 Computerized Generation of Inspection Reports
15 Improved System for Tracking Inventory of Hazardous Wastes

BLANK PAGE

Fast Three-Dimensional-Imaging Camera

The output level of each pixel represents the direction toward an illuminated object.

Marshall Space Flight Center, Alabama

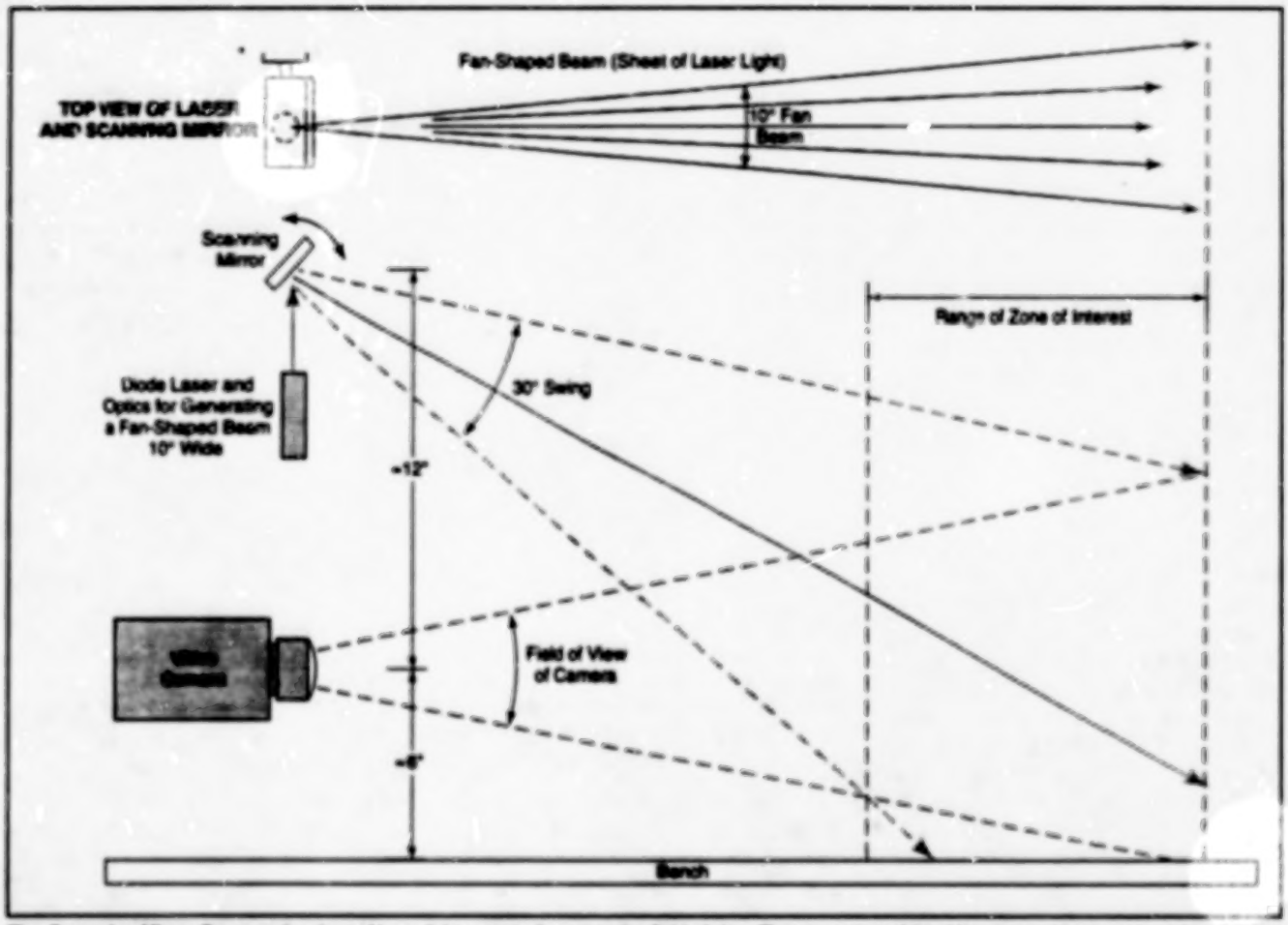
Fan-Shaped Beam (Sheet of Laser Light)
TOP VIEW OF LASER AND SCANNING MIRROR
10° Fan Beam
Scanning Mirror
Range of Zone of Interest
Diode Laser and Optics for Generating a Fan-Shaped Beam 10° Wide
30° Swing
+12°
Field of View of Camera
-6°
Bench

The Scanning Mirror Sweeps the sheet of laser light repeatedly across the field of view. The raw output of the video camera is not a conventional video signal, but rather, one in which the voltage for each pixel is indicative of the scan angle at which the object point imaged on the pixel was illuminated.

The Fast 3D Imaging (F3DI) camera is a developmental system that measures the three-dimensional coordinates of objects within its field of view at distances up to a few feet. The F3DI camera comprises analog and digital electronic, electromechanical, and optical subsystems that function together to generate a range image and/or the digital-data equivalent of a range image. (A range image resembles a conventional video image except that the brightness of each pixel represents the distance to the nearest object point along the line of sight intercepted by that pixel.) A prototype of the system operates at a selectable frame rate up to about 30 Hz.

This system is based on triangulation, using (1) a laser and optics that form the laser beam into a fanlike sheet that projects a line of light onto the nearby scene and (2) a video camera with a field of view that intersects the sheet of light. The distance to an illuminated point of an object imaged onto a given pixel is readily computed from (1) the known baseline distance between the video camera and the laser illuminator, (2) the known direction of the line of sight between the pixel and the illuminated point, and (3) the known orientation of the sheet of light with respect to the baseline and the line of sight.

As described thus far, this system is similar to some other video ranging systems based on triangulation. However, this system implements the triangulation principle in unique ways. The laser illuminator includes a scanning mirror that, during each frame period, sweeps the fan-shaped laser beam through a 30° angular interval that crosses the field of view of the camera (see figure). A shaft-angle encoder monitors the scan angle, and associated circuitry generates a scan-synchronized ramp voltage waveform; that is, the instantaneous voltage of this waveform is indicative of the instantaneous scan angle.

The video camera is of the charge-coupled-device (CCD) type, but with modifications to perform some nontraditional imaging functions. The circuitry in each pixel in the camera includes electronic switches and a capacitor that, together, act as a sample-and-hold device. At the beginning of each frame period, a synchronizing pulse from the scanning-control circuitry causes one electronic switch to discharge the capacitor, then the capacitor-discharging electronic switch is opened and a capacitor-charging switch is closed.

Then as the scan progresses, the capacitor is charged with the ramp voltage. The photodetector in each pixel is used, not to measure the local image brightness, but, rather, as a threshold triggering device; when the fan laser beam crosses the point in the scene corresponding to the pixel, light reflected from that point is focused onto the

pixel by the camera lens, and the amplified output of the photodetector in the pixel causes the capacitor-charging electronic switch to open. Thus, the charge on the capacitor is frozen at a voltage representative of the scan angle. This charge constitutes the CCD pixel readout signal for the frame period. The readout signals from all the pixels are digitized and used, along with pixel locations, to address an electronic lookup table that contains precomputed relationships among ramp voltages, scan angles, lines of sight, pixel positions, and ranges. The lookup process can be accomplished in a fraction of a microsecond on a typical computer. The results of the lookup can be processed into a range image or presented as digital range data.

This work was done by Leonard S. Haynes of Intelligent Automation, Inc., and Rudy Dyck for **Marshall Space Flight Center**. *Further information is contained in a TSP [see page 1].*
MFS-26484

Improved Ultraviolet-and-Infrared Hydrogen-Flame Detector

Small hydrogen flames can be distinguished from other sources of light.

John F. Kennedy Space Center, Florida

An optoelectronic instrument for detecting small hydrogen flames includes analog and digital circuitry (see figure) that processes the outputs of two infrared photodetectors and an ultraviolet photodetector to determine whether a small hydrogen fire lies within its field of view. As in the case of commercial ultraviolet-and-infrared hydrogen-fire detectors, the design of this instrument reduces the incidence of false alarms by taking advantage of the fact that hydrogen fires emit flickering light in both ultraviolet and infrared spectral bands, whereas other sources that one does not seek to detect emit only steady light (e.g., hot objects and reflections of sunlight) or else flicker in the ultraviolet only (e.g. welding arcs and lightning).

This instrument offers an advantage over the commercial units in that its overall design, including its digital-signal-processing algorithm has been formulated, on the basis of experimental observations, to provide reliable detection of a small hydrogen flame within its field of view while reducing the probability of a false alarm from hydrocarbon flames and from moving people and animals. The design also suppresses false alarms that would otherwise be caused by light from a large nearby hydrogen flame that one does not seek to detect because it has been lit deliberately: it does this by distinguishing between the faster fluctuation of light from the small hydrogen flame and the slower fluctuation of light from the larger flame.

In the experiments that guided the formulation of the design, it was observed that when the radiation incident on the infrared and ultraviolet detectors originated from the same hydrogen flame and came directly from that flame (rather than by way of reflection), the time-domain cross-correlation of the output waveforms of the infrared and ultraviolet detectors indicated a high degree of similarity between the waveforms. When the detectors were also receiving light from other sources, the cross-correlation indicated that the waveforms differed. In addition, frequency analysis of the infrared waveforms showed that in the particular application, the flicker of the large flame was concentrated at frequencies < 5 Hz, while the flicker of the small flame extended to tens of hertz.

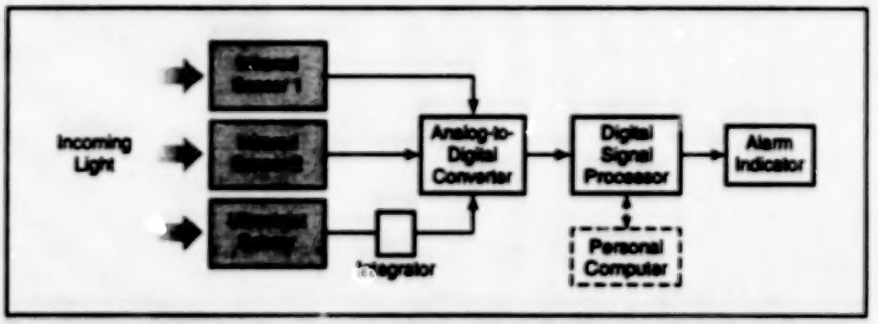

The Improved Hydrogen-Fire Detector includes circuits that process the outputs of ultraviolet- and infrared-photodetector outputs to extract cross-correlations and frequency characteristics indicative of small hydrogen fires. The connection to the personal computer is made, when needed, to change alarm-condition correlation thresholds.

In the operation of the instrument, the output of the ultraviolet detector, which is originally a series of pulses, is integrated to convert it into a continuous signal. The integrated output of the ultraviolet photodetector and the outputs of the two infrared photodetectors are sent to an analog-to-digital converter. The digitized signals are sent to a digital signal processor that computes the frequency spectrum of the flickering of the ultraviolet and infrared signals. The digital signal processor also computes the cross-correlation of the ultraviolet and the infrared signals.

If the analysis of the flicker indicates that light from the large flame is being received either directly or by reflection, the signals are high-pass filtered so that only frequency components of flicker above 5 Hz are used to compute the cross-correlation. If the cross-correlation is larger than a preset threshold between 0.5 and 0.6 (a correlation value of 1.0 indicates identical waveforms) and if the analysis of the flicker indicates that the source of the radiation is a small flame rather than the large one, an alarm is generated.

The alarm condition is updated repeatedly every 2 seconds: The cross-correlation at any given time is computed on the ultraviolet and infrared signals received during the preceding two seconds. When the cross-correlation value falls below a threshold level between 0.3 and 0.4 after having previously triggered an alarm, the alarm is terminated.

This work was done by Gregory A. Hall of **Kennedy Space Center** *and Pedro J. Medelius and Howard James Simpson of I-NET. Further information is contained in a TSP [see page 1].*

This invention has been patented by NASA (U.S. Patent No. 5,625,142). Inquiries concerning nonexclusive or exclusive license for its commercial development should be addressed to the Patent Counsel, Kennedy Space Center [see page 1]. Refer to KSC-11775.

Computerized Generation of Inspection Reports

Pen-based computers running special-purpose software serve as input devices in a computerized inspection-data-recording system. The system was developed to speed inspections, promote consistency of inspection data, facilitate verification of the data, and provide for the printing of inspection reports in a standard format. Previously, inspectors had followed an error-prone, time-consuming procedure in which they recorded their observations in handwritten notes and sketches on paper. Designed specifically for inspections of the thermal protection system on space shuttles, the inspection system could likely be adapted, with modifications, to enhance productivity in other situations in which many inspection reports must be processed. The software provides pop-up menus for primary input. These menus help to reduce errors by restricting an inspector to displayed standard choices. Elements of artificial intelligence in the software automatically reconfigure the pop-up menus on the basis of selected input from an inspector (for example, to present choices that pertain only to the area currently under examination); this feature also helps to prevent errors. An on-screen pop-up keyboard is also available for entry of alphanumerical data. An inspector must still make sketches, but now does so directly on the computer screen for immediate digital recording; thus, images can later be retrieved and printed out quickly and easily.

This work was done by Stephen M. Schneider and Daniel B. Mondshein of United Space Alliance for **Kennedy Space Center**. *Further information is contained in a TSP [see page 1].*

Inquiries concerning rights for the commercial use of this invention should be addressed to the Patent Counsel, Kennedy Space Center [see page 1]. Refer to KSC-11898.

Improved System for Tracking Inventory of Hazardous Wastes

An improved computerized system for tracking an inventory of hazardous wastes has been developed to replace an older tracking system in which manually generated reports were entered manually into computers. The older system required labor-intensive, time-consuming procedures and was prone to errors and delays; the improved system overcomes these disadvantages and affords the additional advantages of standardization and centralization. As in the system described in the preceding article, the points of contact with human technicians are pen-based computers that run special-purpose software that provides pop-up menus, bar codes, buttons, and other interactive displays for entry of data in standard formats. These computers are carried in the field and used to record such data as locations, amounts, and types of wastes. These computers also provide on-line access, in the field, to more than 250 packages of information on the proper technical responses to hazardous-waste situations.

This work was done by Thomas D. Adamson and Stephen M. Schneider of Lockheed Martin Space Operations for **Kennedy Space Center**. *Further information is contained in a TSP [see page 1].*

Inquiries concerning rights for the commercial use of this invention should be addressed to the Patent Counsel, Kennedy Space Center [see page 1]. Refer to KSC-11900.

BLANK PAGE

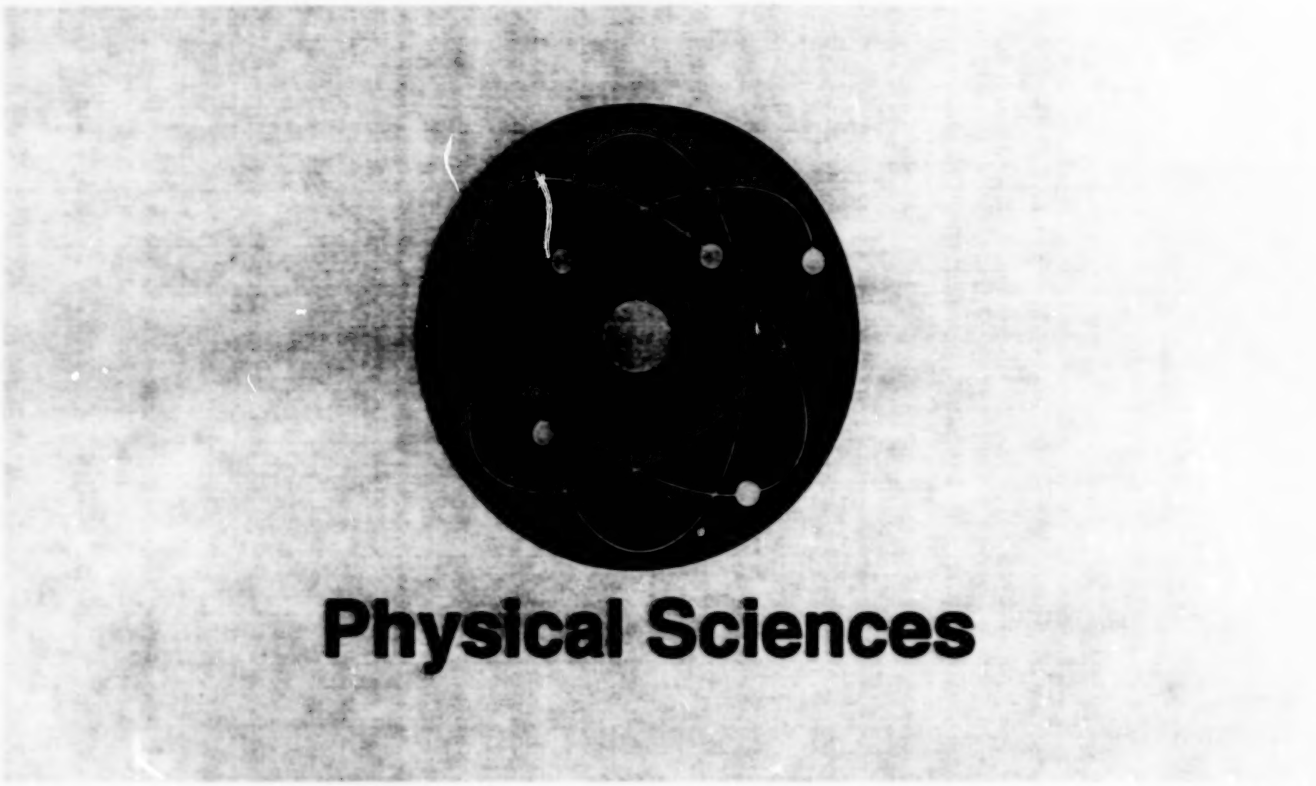

Physical Sciences

Hardware, Techniques, and Processes

19 Determining Temperatures From Hues of Liquid Crystals
20 Alternating-Precessive-Slab Laser Preamplifier
21 Acoustic Wind-Velocity Analyzer
22 Improved Determination of Si in Bi Borosilicate Glass
23 Direct Time Integration of Maxwell's Equations
24 Electronic "Noses" Made From Conductive Polymeric Films
25 Quality/Flowmeter for Two-Phase Fluid
27 Miniature, Low-Power Alphatron
28 Micromechanical Oscillating Mass Balance
29 Polarization-Insensitive Electro-Optical Modulator Systems
30 One-Sided Focusing Schlieren System With Reflective Grid
31 First-Order Modeling of a Radiometer in Mathcad
32 Identifying Electric-Charge Locations With Potential To Generate Lightning
32 Light-Scattering Measurements of Regression of Fuel Droplets

BLANK PAGE

Determining Temperatures From Hues of Liquid Crystals

A nearly linear relationship between hue and temperature was observed in an experiment.

Lewis Research Center, Cleveland, Ohio

Preliminary experiments have demonstrated the feasibility of a colorimetric technique for measuring the temperature of a surface coated with liquid crystals in a suitable binder. The technique could be used to map temperatures relatively noninvasively and should be particularly useful in experimental investigations of heat-transfer processes.

The technique is based on the fact that cholesteric and chiral-nematic liquid crystals progressively exhibit all colors of the visible spectrum as they are heated through certain temperature ranges. The upper and lower limits of the temperature range of a given liquid-crystal mixture can be chosen by selection of the appropriate liquid-crystal ingredients and the proportions thereof. Overall, color-change temperatures of currently available liquid crystals range from a few degrees below zero to several hundred degrees centigrade, and the color-change range of a liquid-crystal mixture can be made as narrow as 1 °C or as wide as 50 °C.

Though the implementation of the technique involves attention to the many details that affect any colorimetric scheme, the basic principle of operation is simple. The surface to be observed would be coated with a liquid-crystal mixture formulated to change color over the temperature range of interest. The object would be observed by a color video camera. The output of the video camera would be fed to an image processor and computer, which would compute a quantitative measure of the hue of each picture element from the red, green, and blue video signals from that picture element. Then by use of a known relationship between the hue measure and temperature (determined previously by calibration measurements at known temperatures), the temperature of the surface point represented by each picture element could be computed. Picture elements at the same temperature could be connected by lines to form isotherms, generating a temperature-contour map of the observed surface.

The upper part of the figure illustrates schematically an apparatus used to demonstrate the technique. The lower part of the figure presents the results of a set of measurements taken on the apparatus. These results confirm the close correspondence between hue and temperature for the particular liquid-crystal tested: particularly noteworthy is the nearly linear change of hue from 35.3 to 36.3 °C. This linear range spans the visible spectrum from red to blue, and the uncertainty band around any given hue value in the linear range is about 0.1 °C wide.

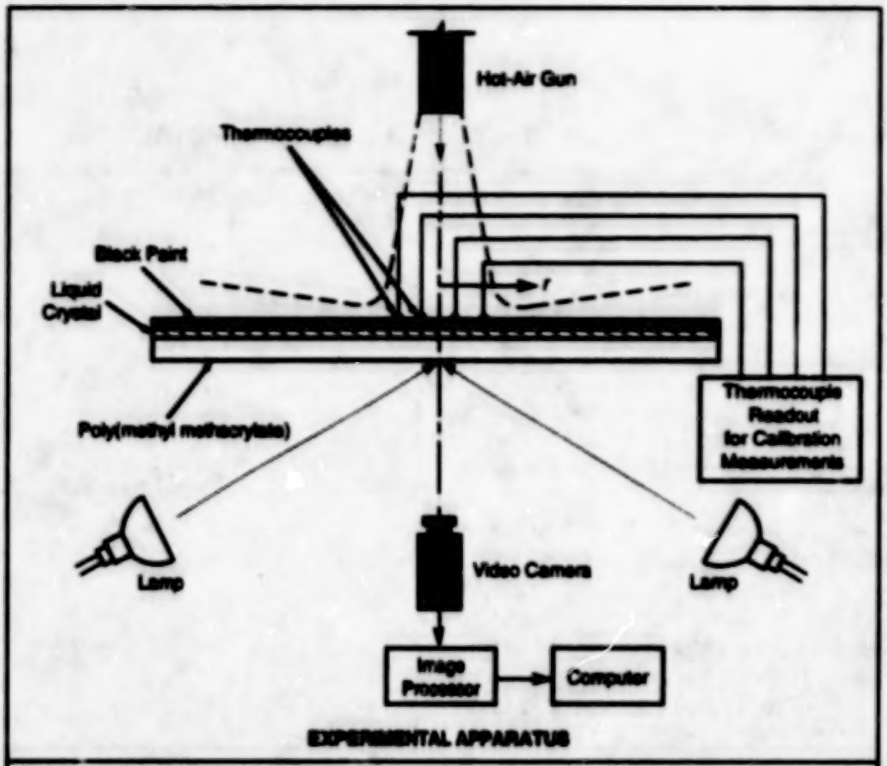

The Video Camera Observes a surface covered with liquid crystals. A temperature map of the surface can be generated by computing hues from the color video output and by using the relationship between temperature and the hue of the liquid crystals.

The preliminary experiments also showed that, as one would expect, the hue-vs.-temperature relationship can change slightly with intensity of illumination and can change to a greater degree with the angle of illumination. Therefore, to minimize the uncertainty in the measurement of temperature, one should set the

lamps at the same distance and angle from the observed surface during both calibration and subsequent measurements to determine unknown temperatures. Also to minimize the uncertainty, one should keep all camera adjustments (gain, zoom, aperture, and the like) and all image-processor color-capturing adjustments the same during calibration and subsequent measurements.

This work was done by Cengiz Camci of Pennsylvania State University and Kuisoon Kim of Pusan National University (Korea) for **Lewis Research Center.**

Further information is contained in a TSP [see page 1].

Inquiries concerning rights for the commercial use of this invention should be addressed to the Patent Counsel, Lewis Research Center [see page 1]. Refer to LEW-15260.

Alternating-Precessive-Slab Laser Preamplifier

The size and the number of components would be minimized.

Goddard Space Flight Center, Greenbelt, Maryland

A laser preamplifier for a pulsed-laser ranging system amplifies pulses with a wavelength of 1,064 nm, duration of < 100 ps, and repetition rates of up to 5 kHz. The preamplifier features a compact design with a minimum number of optical components and simplicity of alignment. Using typical design parameters, the entire preamplifier could fit in a box about the size of a human hand.

The design concept is derived from common laser amplifiers that feature zigzag optical paths and external beam-steering optics to increase gain lengths. In this preamplifier, the amplified laser pulse is kept in the gain medium as long as possible, without need for external beam-steering optics. The gain of this preamplifier is comparable to that of a typical multipass zigzag amplifier with external beam-steering optics.

The design of this amplifier is called "alternating precessive slab" for reasons that will become apparent. The gain medium is a rectangular slab of 1-percent-doped neodymium: yttrium aluminum garnet (Nd:YAG) crystal, which lases at the desired wavelength of 1,064 nm and has an absorption spectral peak at 809 nm. Input and output faces are cut at two corners of the slab and coated for low reflectivity at 1,064 nm. The other faces are coated for high reflectivity at 1,064 nm and low reflectivity at 809 nm. The path traced by the laser pulse in traversing the slab (see Figure 1) includes internal reflections at a succession of points along each side, so that, in a sense, the path precesses around the slab. The design is characterized as "alternating" because the location of the output face alternates between opposite corners if the design parameters were changed in such a way as to make *N* (the number of *x*- or *y*-oriented segments of the path) alternate between even and odd values.

Typically, the overall dimensions of the slab are about 1 by 1 by 0.2 cm. The exact

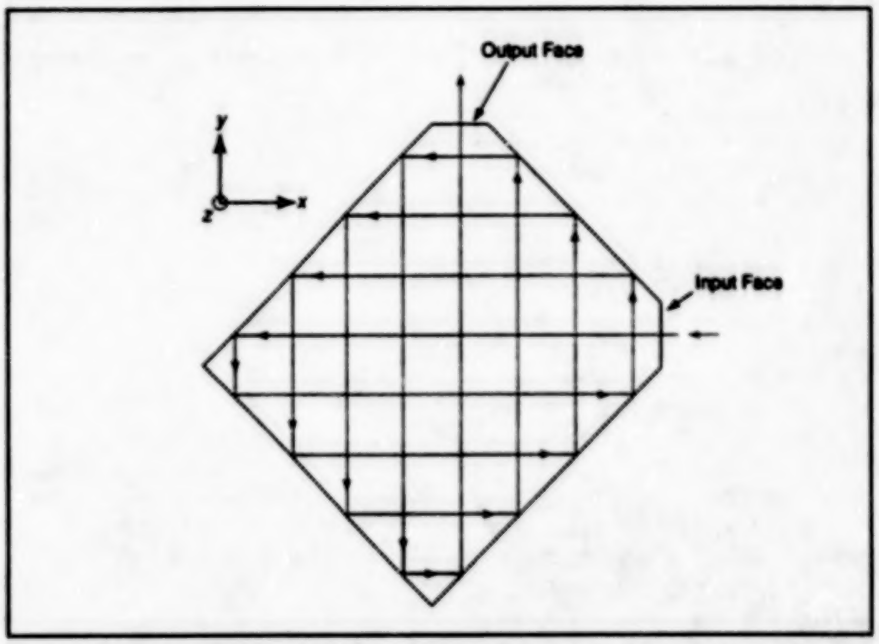

Figure 1. The Optical Path Would Be Folded into a pattern that would keep the laser pulse in the rectangular slab (the gain medium) as long as possible.

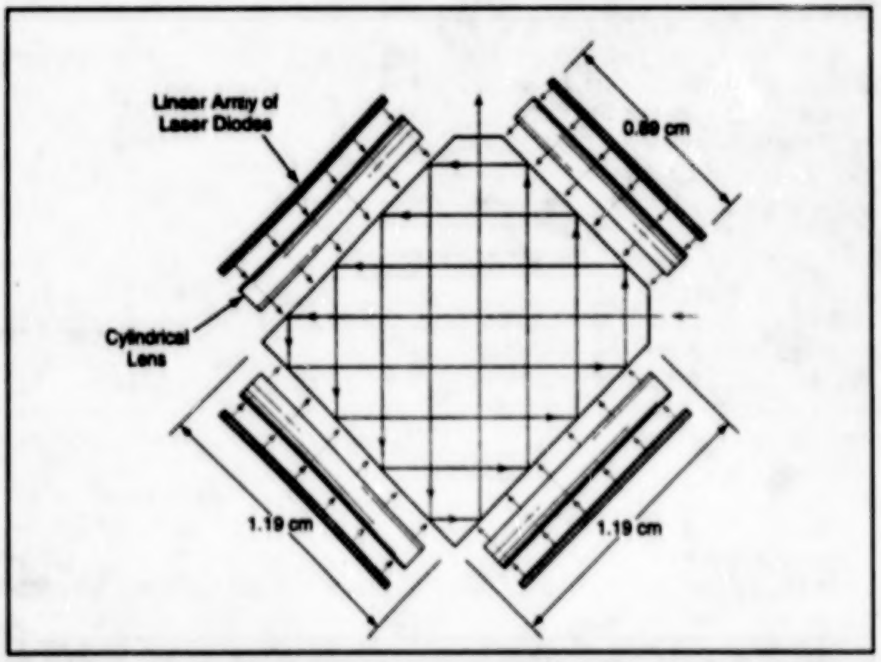

Figure 2. The Gain Medium Could Be Optically Pumped from four sides. Each array of laser diodes would typically operate at a power of 15 W each.

dimensions must be chosen to obtain the desired N and to satisfy other requirements. The slab must be thick enough to accommodate the cross section occupied by the laser pulse (in effect, the width of the laser beam). The choice of thickness is also affected by partially conflicting requirements related to coupling efficiency, diffraction, and quality of the output beam.

The path in the slab must be laid out to prevent overlapping of the cross sections from adjacent path segments.

The slab could be optically pumped according to any of several alternative optical-pumping schemes. For example, as shown in Figure 2, pump light could be generated on four sides by linear arrays of continuous-wave (CW) laser diodes and collimated into the slab by cylindrical lenses.

This work was done by D. Barry Coyle of The American University for **Goddard Space Flight Center**. *Further information is contained in a TSP (see page 1).*
GSC-13326

Acoustic Wind-Velocity Analyzer

The measurements are inherently compensated for variations in atmospheric conditions.

NASA's Jet Propulsion Laboratory, Pasadena, California

An instrument performs acoustic measurements to determine the velocity of the wind in a plane. More specifically, the instrument measures the apparent speeds of propagation of sound through the wind along two known perpendicular directions in the plane. The speed and direction of the wind can then be determined from the known relationships between these speeds and the speed of sound in still air. Because the instrument also measures the speed of sound in a sample of air shielded from the wind, the measurements are inherently compensated for variations in temperature, pressure, humidity, and other atmospheric conditions.

The instrument, illustrated schematically in Figure 1, includes transmitting acoustic transducer A, plus receiving acoustic transducers B, C, and D. The line from A to C (along the y axis) is perpendicular to the line from A to B (along the x axis), and both these lines are exposed to the wind. The line from A to D is shielded from the wind.

The time for a sinusoidal signal to propagate from an acoustic emitter located at position A to reach the three microphones (acoustic receivers) located at B, C, and D is measured. The three propagation times are determined by comparing their received sine waves and their respective zero-crossing times (phase measurement) to the zero-crossing time of a reference sinusoidal signal. The distance from the center of the emitter to each of the microphones is known, and therefore, the velocity vectors v_{AB}, v_{AC}, and v_{AD} are determined. The speed of sound in still air, v_{AD}, is known because the path AD is shielded from the wind.

Figure 2 illustrates the computation of velocity. Let w = the speed of the wind. To first order in w/v_{AD}, the speed of sound along each of the two perpendicular paths through the wind equals the speed of sound in still air plus the component of wind velocity along that path. Thus, the two perpendicular components (w_x, w_y) of wind velocity can be obtained from $w_x = v_{AB} - v_{AD}$ and $w_y = v_{AC} - v_{AD}$. Then the speed of the wind is given by

$$w = \left(W_x^2 + W_y^2\right)$$
$$= \left[\left(v_{AB} - v_{AD}\right)^2 + \left(v_{AC} - v_{AD}\right)^2\right]$$

and the angle, ϕ, of the wind relative to the x axis is given by

$$\phi = \tan^{-1}\left(w_y / w_x\right) = \tan^{-1}$$
$$\left[\left(v_{AC} - v_{AD}\right)/\left(v_{AB} - v_{AD}\right)\right]$$

The instrument operates under control by a microprocessor, and a microprocessor performs the velocity computations. These and other features make the instrument competitive with conventional mechanical wind-measurement devices. Moreover, microprocessor circuitry provides an interface with external electronic data-processing equipment.

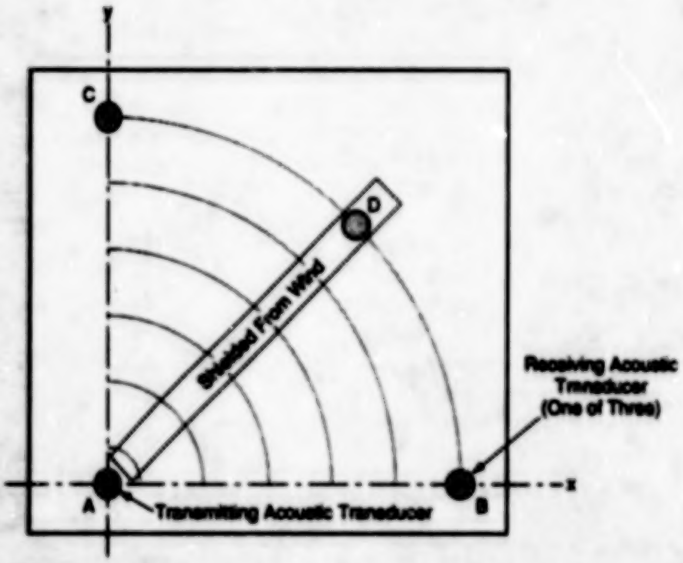

Figure 1. The Acoustic Transducers are used to measure the speeds of sound along the x and y paths exposed to the wind and along a third path shielded from the wind.

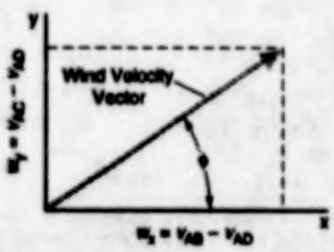

Figure 2. The Velocity Computations are based on simple linear superposition of sound-velocity and wind-velocity vectors.

This work was done by David W. Juergens of Caltech for **NASA's Jet Propulsion Laboratory**. *Further information is contained in a TSP (see page 1).*
NPO-19478

Improved Determination of Si in Bi Borosilicate Glass

A flow-injection spectrophotometric method eliminates interference by bismuth.

Lewis Research Center, Cleveland, Ohio

A laboratory method that includes flow-injection spectrophotometry has been devised for measuring the silicon contents of borosilicate glasses and ceramics that contain bismuth. The determination of the concentrations of the chemical components of glasses and ceramics is essential for correlation of physical properties with chemical compositions. Numerous chemical-analysis procedures for determining the concentrations of typical chemical components of glasses and ceramics are available; some of these procedures are free from interferences, while others are subject to interferences that result in erroneously high or low values.

Inductively coupled argon plasma emission spectroscopy (ICAP) is usually reported to be free of interferences among the three primary elements (Bi, B, and Si) in bismuth borosilicate glass. However, elevated values attributable to interferences were obtained in an experiment: A series of bismuth borosilicate glasses were prepared starting with known composition, and samples of these glasses were submitted for elemental analysis by ICAP. The Bi and B values obtained in the ICAP analysis were acceptably close to the expected values, but the Si values from most samples were almost always elevated; in the worst case, the ICAP value for Si was 911 percent of the proportion (2.1 percent) used in preparing the sample. These results were unacceptable and therefore it became necessary to develop a method to make it possible to confirm the ICAP determinations.

Flow-injection spectrophotometry, on which the present method is based, is an alternative method of determining the concentrations of chemical components in a procedure that involves development of color in a carrier line, followed by spectrophotometric determination of the color. The dissolved sample is injected into a carrier line that contains one or more substance(s) that react with the sample, rendering a colored product. One of the oldest and most widely used methods for the determination of silicon in the form of silicate involves the formation of the heteropoly complex with molybdate, followed by the reduction of the complex to heteropoly blue, which is an intensely colored material. The majority of the flow-injection methods reported in the literature incorporate additional reagents for the suppression of phosphate and other interferences, but none of these methods prevents interference by precipitation of bismuth.

BISMUTH INTERFERENCE:

$Bi^{3+} + OH^- + F^-$ or $Cl^- \rightarrow$ BiOF or BiOCl (Turbid Precipitate)

REMOVAL OF BISMUTH INTERFERENCE:

$Bi^{3+} + OH^- + EDTA^{4-} \rightarrow BiEDTA^-$ (Colorless Solution)

FLUORIDE INTERFERENCE:

$SiO_3^{2-} + F^- \rightarrow SiF_6^{2-}$

$SiF_6^{2-} + MoO_4^{2-} \rightarrow$ No Color-Forming Reaction

REMOVAL OF FLUORIDE INTERFERENCE:

$SiF_6^{2-} + BO_3^{3-} \rightarrow BF^- + SiO_3^{2-}$

$SiF_6^{2-} + Al^{3+} \rightarrow AlF_6^{3-} + SiO_3^{2-}$

$SiO_3^{2-} + MoO_4^{2-} \rightarrow$ Colored Heteropoly Complex

Figure 1. These Chemical Reactions figure in the interferences and the elimination of interferences as described in the text.

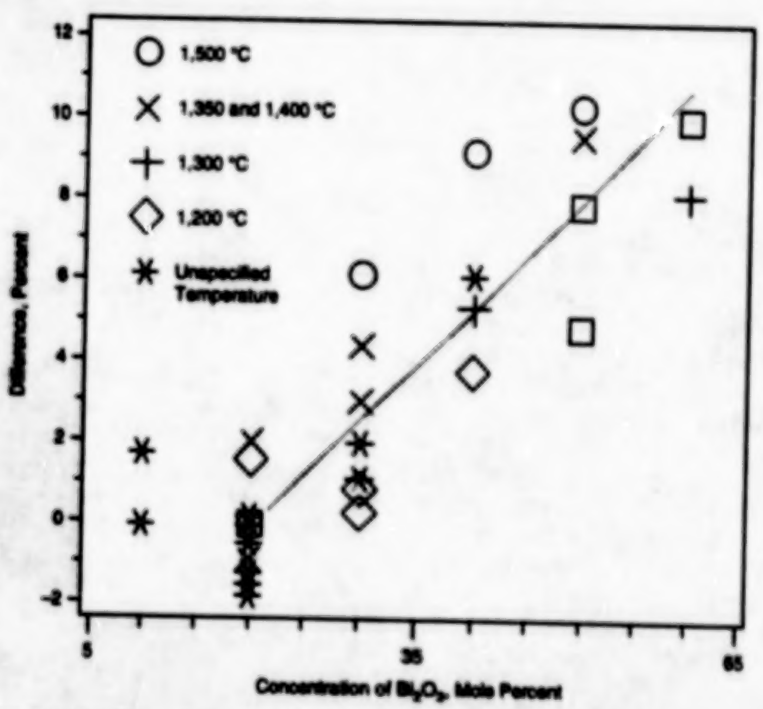

Figure 2. This Plot Shows Differences between the (a) mole percent concentrations of Si determined by the method described in the text and (b) calculated mole percent concentrations of Si as functions of (c) calculated mole percent concentrations of Bi_2O_3 in glass specimens that were fused at various temperatures. The solid line is a regression line through all data points for which the mole percentage of $Bi_2O_3 \geq 20$.

Figure 1 illustrates the unbalanced interference reactions along with reactions to eliminate the interferences. In the present method, the bismuth interference is eliminated in a sample-pretreatment step. The interference from hydrofluoric acid used to dissolve the sample for analysis is removed by a first carrier reagent, which contains an optimized mixture of borate and aluminum sulfate. The flow in the carrier line that contains the first carrier reagent is merged with that in a second line containing a second carrier reagent, which develops the heteropoly blue color prior to flow through the spectrophotometer cell.

In experiments, the determinations made by applying the present method of flow-injection spectrophotometry to samples of bismuth borosilicate glass were found to be comparable to the determinations of the standard ICAP method, confirming that either flow-injection spectrophotometry or ICAP are acceptable methods for determining the concentration of Si in the presence of Bi and B. The modifications of the molybdate reagent and of sample-preparation procedure eliminate the Bi interference and the hydrofluoric acid matrix interferences in the flow-injection procedure.

The preparation of ceramics and glasses routinely includes fusion of the raw materials in crucibles made of a large variety of materials. Bismuth oxide, in addition to being volatile and subliming at moderately low temperatures, is extremely corrosive in its molten state. Crucibles of platinum are dissolved by molten bismuth oxide, and graphite crucibles become degraded, causing graphite particles to be entrapped in the resulting products. Vycor (or equivalent) silica material is only partially attacked by the bismuth flux. From the extensive number of Si determinations in glass samples prepared in Vycor, it is apparent that the Bi_2O_3 content is largely responsible for elevated Si levels and that the level of elevation has a slight dependence on fusion temperature (see Figure 2).

This work was done by Frances A. Archer and Kenneth W. Street, Jr., of **Lewis Research Center**. *Further information is contained in a TSP [see page 1].*

Inquiries concerning rights for the commercial use of this invention should be addressed to the Patent Counsel, Lewis Research Center [see page 1]. Refer to LEW-16098.

Direct Time Integration of Maxwell's Equations

Propagation of optical pulses in a nonlinear medium can be simulated with high accuracy.

Ames Research Center, Moffett Field, California

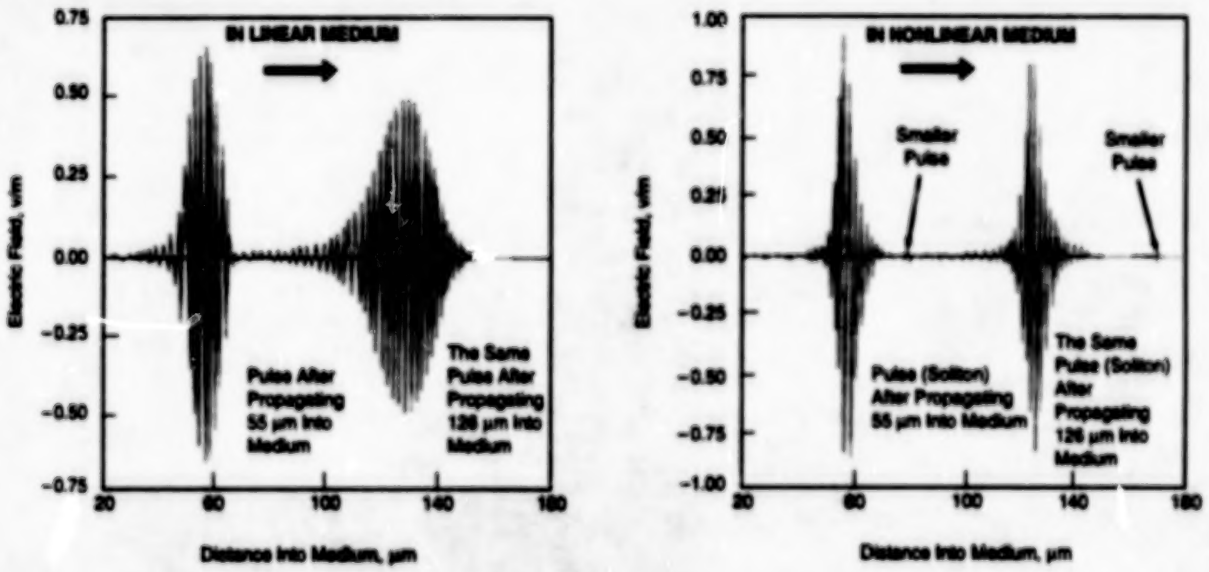
IN LINEAR MEDIUM
Pulse After Propagating 55 μm Into Medium
The Same Pulse After Propagating 126 μm Into Medium
Electric Field, v/m
Distance Into Medium, μm
IN NONLINEAR MEDIUM
Smaller Pulse
Smaller Pulse
Pulse (Soliton) After Propagating 55 μm Into Medium
The Same Pulse (Soliton) After Propagating 126 μm Into Medium
Electric Field, v/m
Distance Into Medium, μm

The Propagation of an Optical Pulse that contained about seven carrier-frequency cycles was simulated. In the linear medium, the pulse was found to undergo dispersion. In the nonlinear medium, the pulse was found to act as a soliton that approximately retained its amplitude and duration. It was also found that a second, smaller pulse formed and moved out ahead of the main soliton pulse.

cal pulses (including electromagnetic solitons) in a nonlinear, dispersive medium can be simulated numerically by means of a method that involves direct time integration of Maxwell's equations. The time integration efficiently implements linear and nonlinear convolutions that appear in expressions for the linear and nonlinear parts, respectively, of the electric polarization of the medium.

The method can be described in terms of its application to a one-dimensional test case in which a pulse of light propagates along the z axis in an x, y, z Cartesian coordinate system into a half space ($z > 0$) filled with a homogeneous, isotropic, nonmagnetically-permeable nonlinear dielectric medium. The electric-field, magnetic-field, and electric-displacement vectors are taken to have components E_x, H_y, and D_x, respectively, where the subscripts denote the directions. The applicable set of Maxwell's equation is

$$\frac{\partial H_y}{\partial t} = \frac{1}{\mu_0}\frac{\partial E_x}{\partial z}, \quad \frac{\partial D_x}{\partial t} = \frac{\partial H_y}{\partial z},$$

$$\text{and } E_x = \frac{D_x - \left(P_{xL} + P_{xNL}\right)}{\varepsilon_0}$$

where t denotes time; ε_0 and μ_0 denote the electric permittivity and magnetic permeability, respectively, of the vacuum; and P_{xL} and P_{xNL} denote the linear and nonlinear parts, respectively, of the electric polarization along the z axis.

P_{xL} is given by the following linear convolution of $E_x(x, t)$ with the linear susceptibility function $\chi^{(1)}$:

$$P_{xL}(x,t) = \varepsilon_0 \int_{-\infty}^{\infty} \chi^{(1)}(t-t')E_x(x,t')dt'$$

In this case, the medium is considered to have a Lorentz linear dispersion characterized by

$$\chi^{(1)}(t) = \frac{\omega_p^2}{\nu_0} e^{-\beta/2} \sin \nu_0 t,$$

which is equivalent to a dielectric permit-

tivity, ε, as a function of angular frequency, ω, given by

$$\varepsilon(\omega) = \varepsilon_\infty + \frac{\omega_0^2(\varepsilon_s - \varepsilon_\infty)}{\omega_0^2 - j\delta\omega - \omega^2}$$

where ω_0 denotes a resonant frequency, δ denotes a coefficient of damping, and the other parameters are related by

$$\omega_p^2 = \omega_0^2(\varepsilon_s - \varepsilon_\infty)$$

and

$$\nu_0^2 = \omega_0^2 - \frac{\delta^2}{4}$$

P_{phL} is given by the following nonlinear convolution of $E_z(x, t)$ with the third-order susceptibility function $\chi^{(3)}$:

$$P_{phL}(x,t) = \varepsilon_0 \int_{-\infty}^{\infty}\int_{-\infty}^{\infty}\int_{-\infty}^{\infty} \chi^{(3)}(t-t_1, t-t_2, t-t_3) \times E_z(x,t_1) E_z(x,t_2) E_z(x,t_3)\, dt_1 dt_2 dt_3$$

The nonlinear convolution provides for nonlinear physical effects with time retardation or memory. In this particular case, the nonlinear properties are characterized by the following single-time nonlinear convolution:

$$P_{phL}(x,t) = \varepsilon_0 \chi^{(3)} E_z(x,t) \times \int_{-\infty}^{\infty} \left[\alpha\delta(t-t') + (1-\alpha) g_R(t-t')\right] \times E_z^2(x,t')\, dt'$$

In this equation, $\chi^{(3)}$ becomes a constant coefficient of the nonlinear susceptibility, $\delta(t)$ models Kerr nonresonant virtual electronic transitions on the order of about 1 fs or less, $g_R(t) = [(\tau_1^2 + \tau_2^2)/\tau_1\tau_2^2]e^{-t/\tau_2}\sin(t/\tau_1)$ and models transient Raman scattering, and α parameterizes the relative strengths of the Kerr and Raman interactions. Effectively, $g_R(t)$ models a single Lorentzian spectral line that is centered on the optical-phonon frequency $1/\tau_1$ and has a bandwidth of $1/\tau_2$ (the reciprocal phonon lifetime).

The formulation of the linear and nonlinear convolutions is completed by assuming that the electromagnetic field is zero at $t \le 0$ and by defining

$$F(t) = \varepsilon_0 \int_0^t \chi^{(1)}(t-t') E_z(x,t')\, dt'$$

and

$$G(t) = \varepsilon_0 \int_0^t g_R(t-t') E_z^2(x,t')\, dt'$$

It can be shown that F and G satisfy the following coupled nonlinear ordinary differential equations:

$$\frac{1}{\omega_0^2}\frac{d^2F}{dt^2} + \frac{\delta}{\omega_0}\frac{dF}{dt} + \left[1 + \frac{\varepsilon_s - \varepsilon_\infty}{\varepsilon_\infty + \alpha\chi^{(3)}E_z^2}\right]F + \frac{(\varepsilon_s - \varepsilon_\infty)(1-\alpha)\chi^{(3)}E_z G}{\varepsilon_\infty + \alpha\chi^{(3)}E_z^2} = \frac{(\varepsilon_s - \varepsilon_\infty)D_z}{\varepsilon_\infty + \alpha\chi^{(3)}E_z^2},$$

and

$$\frac{1}{\omega_0^2}\frac{d^2G}{dt^2} + \frac{\bar{\delta}}{\bar{\omega}_0^2}\frac{dG}{dt} + \left[1 + \frac{(1-\alpha)\chi^{(3)}E_z^2}{\varepsilon_\infty + \alpha\chi^{(3)}E_z^2}\right]G + \frac{E_z F}{\varepsilon_\infty + \alpha\chi^{(3)}E_z^2} = \frac{D_z E_z}{\varepsilon_\infty + \alpha\chi^{(3)}E_z^2}$$

where

$$\bar{\delta} = \frac{2}{\tau_2} \text{ and } \bar{\omega}_0^2 = \frac{1}{\tau_1^2} + \frac{1}{\tau_2^2}$$

These equations are first solved simultaneously for F and G at the latest time step by use of a second-order-accurate finite-difference scheme that operates on data for the current value of D_z and previous values of D_z, E_z, F, and G. Only two time steps of storage are needed in this approach. Then the latest value of E_z can be obtained by Newton's iteration of the following equation, using the new values of D_z, F, and G:

$$E_z = \frac{D_z - F - (1-\alpha)\chi^{(3)}E_z G}{\varepsilon_0\left(\varepsilon_\infty + \alpha\chi^{(3)}E_z^2\right)}$$

Once the E_z field has been computed, H and D_z can be computed from E_z by use of Maxwell's equations. The figure illustrates some results obtained by applying this method to two versions of the test case.

This work was done by Peter Goorjian of **Ames Research Center** *and Allen Taflove of Northwestern University. Further information is contained in a TSP [see page 1].*

Inquiries concerning rights for the commercial use of this invention should be addressed to the Patent Counsel, Ames Research Center [see page 1]. Refer to ARC-13259.

Electronic "Noses" Made From Conductive Polymeric Films

Arrays of multiple sensors would be used to distinguish among different vapors.

NASA's Jet Propulsion Laboratory, Pasadena, California

Broadly responsive, low-power electronic chemical-vapor sensors called "chemiresistors" are undergoing development. A chemiresistor comprises a pair of metal electrodes in contact with a thin, electrically conductive modified polypyrrole film on an electrically insulating substrate. The electrical resistivity of the film increases or decreases reversibly when the film is exposed to a chemical vapor or vapors. Multiple chemiresistors can be assembled into arrays, within which each chemiresistor is maximally responsive to a different chemical or mix of chemicals.

The film in a chemiresistor is made by chemical polymerization of a pyrrole with phosphomolybdic acid (which serves as an oxidizing and polymerizing agent), along with a plasticizer, all dissolved in tetrahydrofuran. The polymerizing solution is applied to the sensor substrate and polymerization proceeds as the tetrahydrofuran evaporates. Once polymerization is complete, the film is washed with methanol to remove excess phosphomolybdic acid and/or pyrrole monomer.

For a given film, the polymerization conditions and the concentration and type of plasticizer determine the sensory response to a given vapor chemical species or mixture; these parameters can be controlled to obtain a film with a known unique response for use in an array. Thus, an array includes sensory films that contain various plasticizers (see Figure 1).

An array produces a chemically reversible, diagnostic pattern of changes in electrical resistance upon exposure to different odorants. The resistances of the sensors in an array can be monitored, for example, by use of a multiplexing digital ohmmeter, the digital outputs of which are processed together to extract data on the concentration(s) of chemical vapor(s) in the air, somewhat in imitation of the manner in

which the brain recognizes sensory patterns of odors that stimulate multiple olfactory receptors in the nose (see Figure 2).

The resistance readings are taken at selected times before, during, and after exposure of the sensor to air containing the vapor mixture of interest. The change (ΔR) in each resistance from its initial, preexposure value (R) is divided by the initial value, yielding a fractional resistance change ($\Delta R/R$). Then the $\Delta R/R$ values from all the chemiresistors in the array are processed together to determine the concentrations of components of vapor mixtures. As envisioned but not yet implemented, the $\Delta R/R$ values would be processed by a software or hardware neural network to determine the concentrations of components of the vapor mixture.

In initial experiments, an array of 14 chemiresistors was exposed to vapors of acetone, benzene, chloroform, ethanol, isopropyl alcohol, methanol, tetrahydrofuran, and ethyl acetate in air. Principal-component analysis of the $\Delta R/R$ responses showed that the array could be used to distinguish among these vapors and quantify their concentrations. It was also found possible to resolve the components of mixtures of ethanol and methanol vapors. The responses of the chemiresistors were complicated somewhat by temporal variations attributable to water vapor, but these complications did not adversely affect reproducibility and reversibility, and it was still possible to extract data on the responses to the organic solvents of interest. Moreover, the test environment was representative of many practical odor-sensing applications, from which air and water could not be readily excluded.

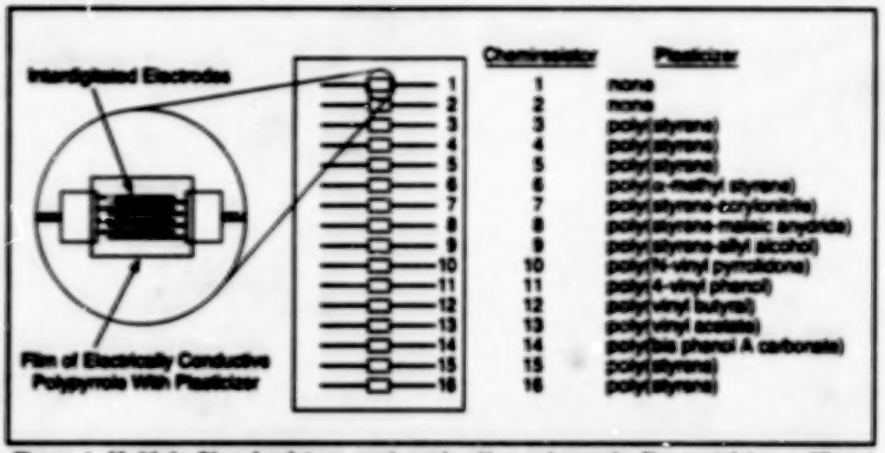

Figure 1. Multiple Chemiresistors, each made with a polypyrrole film containing a different plasticizer, are assembled into an array for sensing a variety of chemical vapors.

This work was done by Nathan S. Lewis and Michael S. Freund of Caltech for **NASA's Jet Propulsion Laboratory.** *Further information is contained in a TSP [see page 1].*

In accordance with Public Law 96-517, the contractor has elected to retain title to this invention. Inquiries concerning rights for its commercial use should be addressed to

Larry Gilbert, Director
Technology Transfer
California Institute of Technology
Mail Code 315 - 6
Pasadena, CA 91125
(818) 395-3288

Refer to NPO-19537, volume and number of this NASA Tech Briefs issue, and the page number.

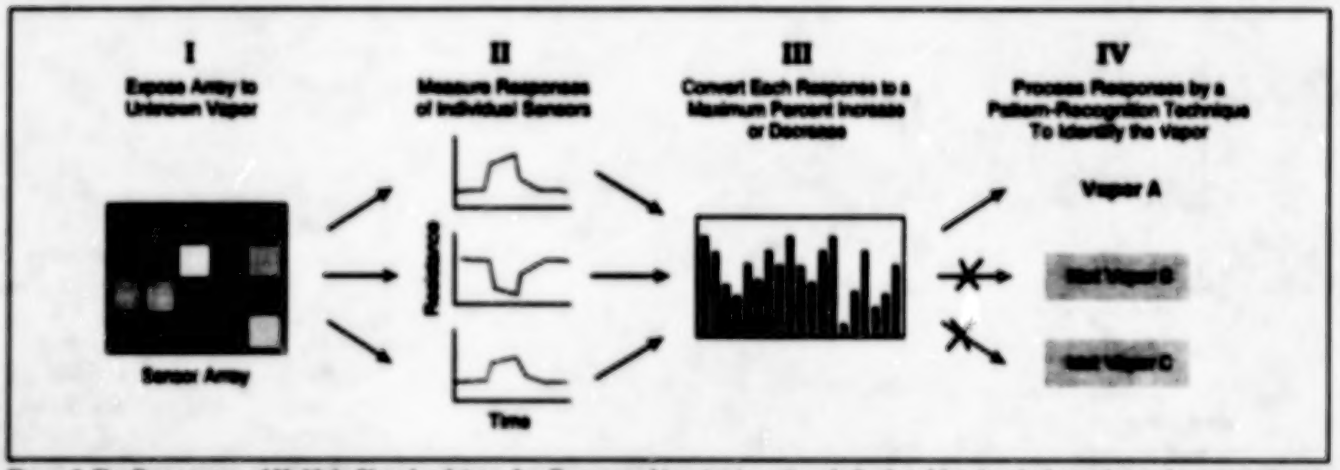

Figure 2. The Responses of Multiple Chemiresistors Are Processed to extract a pattern indicative of the chemical species and concentration(s) of the sensed vapor(s).

Quality/Flowmeter for Two-Phase Fluid

Flow speed is determined by correlating upstream and downstream capacitance measurements.

John F. Kennedy Space Center, Florida

Figure 1 illustrates a prototype instrument for measuring the volume fractions of liquid and gas and the rate of flow of a two-phase fluid. The instrument is called a "quality/flowmeter" because "quality" as used in engineering disciplines concerned with two-phase flow denotes, loosely, volume fractions of liquid or gas. Although designed specifically for measuring flows of cryogenic liquids containing bubbles of their vapors, the instrument could be readily adapted to other two-phase (including liquid/gas, liquid/liquid and liquid/solid) flows like those of water/steam, water/air, oil/water, and liquid/solid food processing mixtures.

Like some other quality meters, this instrument is based on a capacitance-

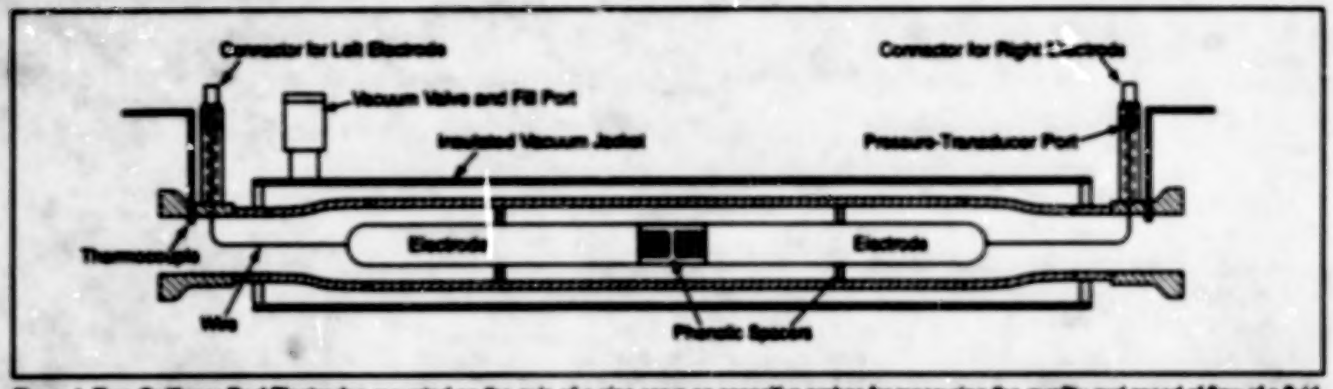

Figure 1. Two Collinear Rod Electrodes mounted on the axis of a pipe serve as capacitive probes for measuring the quality and speed of flow of a fluid in the pipe. A temperature and a pressure sensor provide additional information on the state of the fluid.

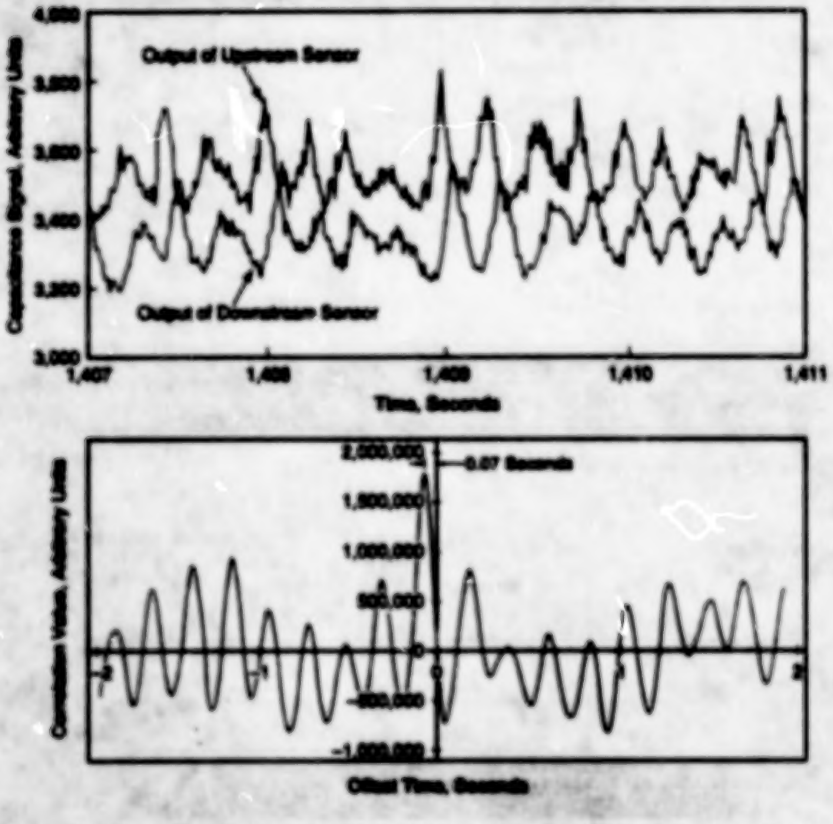

Figure 2. The Correlation Between the Outputs of the upstream and downstream capacitive sensors reaches a peak at an offset time of –0.07 s.

measurement concept: The fluid flows through a space between electrodes, the capacitance between the electrodes is measured, and the volume fractions of liquid and gas are computed from the effective permittivity, using the known relationships (a) between the effective permittivity and the capacitance and (b) between the volume fractions and the effective permittivity. One of the unique features of this instrument is that it contains two capacitive sensors separated from each other by a small distance along the direction of flow. The instrument is built around a section of pipe 32 in. (81.3 cm) long, with a flow cross section 2 in. (5.1 cm) in diameter at the ends. The pipe constitutes a common outer electrode for both capacitive sensors. The other electrodes for the capacitive sensors are metal rods mounted coaxially within the pipe on radial phenolic spacers and separated lengthwise by another phenolic spacer. The pipe tapers to a greater diameter along the length of the electrodes to keep the flow cross section constant along the flow path; this feature helps to minimize the effect of pressure drop. Wires connect the central electrodes to external electrical connectors. A vacuum jacket containing multilayer insulation minimizes heat transfer into the fluid.

The basic idea is to estimate the speed of flow as the quotient of the effective streamwise distance between the capacitive sensors divided by the delay between common features in the outputs of both sensors. The signal features are associated with the sizes and positions of bubbles as they move past the electrodes, and it is assumed that the velocity of each bubble closely approximates the velocity of the surrounding liquid. The two signals can be expected to have some common features — that is, the downstream signal can be expected to be an approximate, delayed version of the upstream signal — provided that the flow is not so turbulent as to alter completely the relative positions of bubbles in the interval between the upstream and downstream sensors.

The capacitance readings are sampled at intervals of less than 1 ms. Correlations between the upstream and downstream readings are computed for a range of offset times, and the delay between the upstream and downstream readings is deemed to be that offset time at which the correlation reaches its peak (see Figure 2).

Another unique feature of this instrument is the incorporation of a temperature and a pressure sensor. The combination of quality, temperature, and pressure data enables a more nearly complete characterization of the fluid. These data can be used to estimate the density. Then the mass flow rate can be estimated from the density, the flow speed obtained from the correlation of capacitance signals, and the geometry of the instrument.

This work was done by James E. Fesmire and Rudy J. Wahnik of **Kennedy Space Center** *and Kenneth A. Rose, William D. Haskell, Robert C. Youngquist, Robert B. Cox, and John S. Moerk of I-NET. Further information is contained in a TSP [see page 1].*

This invention is owned by NASA, and a patent application has been filed. This technology is being further developed through NASA's Dual Use Technology Development Program, where NASA and its partner, Air Products and Chemicals, Inc., are jointly funding the developmental effort. Inquiries concerning the commercial development of this technology should be addressed to the Technology Programs and Commercialization Office, Kennedy Space Center; (407) 867-3017. Refer to KSC-11725.

Miniature, Low-Power Alphatron

This device would fit into a cube of about 1 cm.

NASA's Jet Propulsion Laboratory, Pasadena, California

A proposed gas-pressure gauge of the "alphatron" type would feature unusually wide dynamic range, small size, and low power consumption. Conceived for measuring the pressure of the Martian atmosphere, this gauge could also be used on Earth to measure atmospheric and subatmospheric gas pressures in scientific and industrial apparatus.

Alpha particle vacuum gauges have been out of common use for decades due to lack of a practical technology compatible with workplace safety standards. An alpha particle gauge is an ionization-type pressure gauge (more precisely, a density gauge) in which alpha particles (energetic helium nuclei) from a radioactive source produce positive ions in a gas. An electric field is imposed on the gas by applying a suitable electric potential to a cathode and anode, causing the positive ions to drift to the cathode and electrons to drift to the anode. The ionization current thus collected by the cathode is measured and taken as an indication of the density of the gas (equivalently, the pressure of the gas at a given temperature).

In the proposed miniature alpha gauge (see figure) the alpha particle source would be a small piece of an americium isotope, similar to those used in household smoke detectors. The source would be covered by a gold surface layer to attenuate the alpha particles to an optimum kinetic energy of the order of 1 MeV. The α source would be electrically grounded and located near the center of an annular-disk-shaped cathode. The cathode would be connected to the input pin of an operational-amplifier integrated circuit, making it possible to measure ion current as small as a fraction of a picoampere.

A cylindrical-cup-shaped anode would be placed over the α source and cathode, and would be held at a positive potential. The dimensions of the anode must be chosen, in conjunction with other design parameters, so that at the maximum intended operating gas pressure, the range of the α particles is greater than the distance to the anode. This is important because, if the α tracks terminate within the active volume, then the number of ions produced is independent of pressure, and the sensor would no longer function as a pressure gauge.

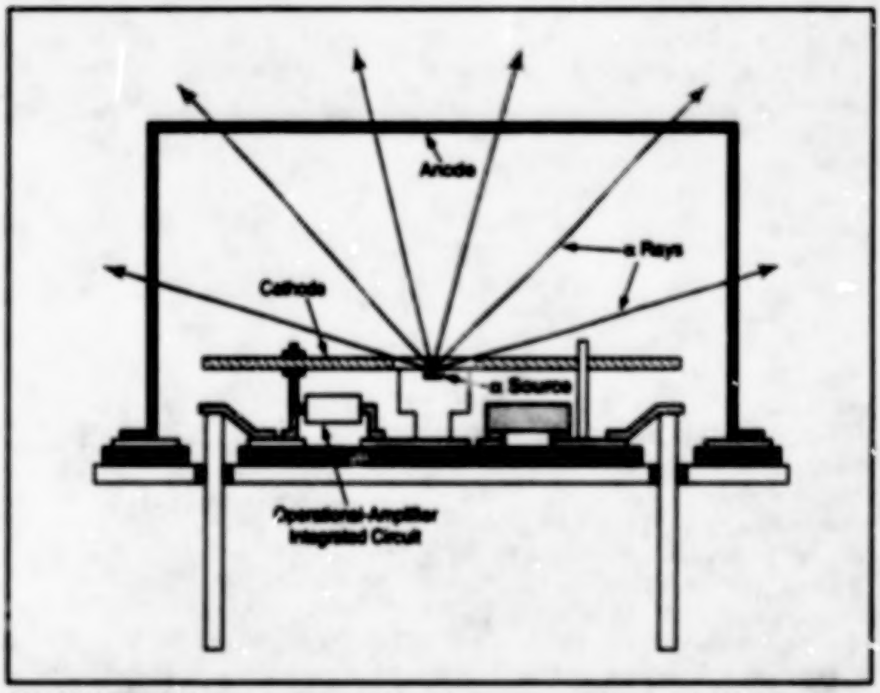

This Miniature Alphatron would respond linearly to pressures from 1 to 1,000 millibars.

Preliminary experiments and design calculations suggest that the ion current would be directly proportional to pressure over the range from 1 to 1,000 millibars (10^2 to 10^5 Pa) at standard temperature. Like other alphatrons, this one would offer the advantages of ruggedness and no moving parts. By use of surface-mount hybrid technology, it should be possible to fit this alphatron within a package of about 1 cm in each linear dimension.

This work was done by Martin G. Buehler, L. Douglas Bell, and Michael H. Hecht of Caltech for NASA's Jet Propulsion Laboratory. Further information is contained in a TSP [see page 1].

In accordance with Public Law 96-517, the contractor has elected to retain title to this invention. Inquiries concerning rights for its commercial use should be addressed to

Larry Gilbert, Director
Technology Transfer
California Institute of Technology
Mail Code 315 - 6
Pasadena, CA 91125
(818) 395-3288

Refer to NPO-19622, volume and number of this NASA Tech Briefs issue, and the page number.

Micromechanical Oscillating Mass Balance

Advantages would include compactness and relative simplicity.

Lyndon B. Johnson Space Center, Houston, Texas

A micromechanical oscillating mass balance has been proposed for measuring small amounts (with resolution of the order of 10^{-6} g) of contaminant material deposited on its surface. As in the case of the commercial quartz crystal microbalances now used as contamination detectors, the contaminant mass would be measured in terms of a small change in the frequency of resonance of mechanical oscillations.

The micromechanical oscillating mass balance would include a conductor/dielectric/conductor laminated composite beam with both ends rigidly fixed (see figure). Typically, the beam would be about 3 mm long, 0.1 mm wide, and 6 μm thick, though of course the dimensions in a specific design could differ considerably from these representative values. The beam would be fabricated by techniques now used in the microelectronics industry and thus could be integrated on a silicon chip along with supporting electronic circuitry. The resonant frequency — that is, the frequency of the fundamental mode of vibration of the beam — would typically be a few kilohertz.

Permanent magnets would be mounted nearby to impose a magnetic field across the beam. An alternating current would be driven along one of the conductive layers on the beam, so that the force produced by the interaction between the current and the permanent magnetic field would set the beam into oscillation at the driving frequency. The oscillating motion of the other conductive layer in the magnetic field would generate alternating voltage between the ends of the beam in that layer; the amplitude of this output voltage could be measured as an indication of the amplitude of vibration.

During a measurement session, the output voltage would be measured as a function of the driving frequency; the resonant frequency would be identified as that driving frequency at which the output voltage reached its peak value. An accumulation of contaminant mass during the time between two measurement sessions would manifest itself as a decrease in the resonant frequency. Theoretical calculations show that a contaminant mass of only 10^{-6} g would decrease the resonant frequency by about 1 Hz in the typical case. Frequency shifts of these magnitudes are easily measurable by currently available equipment.

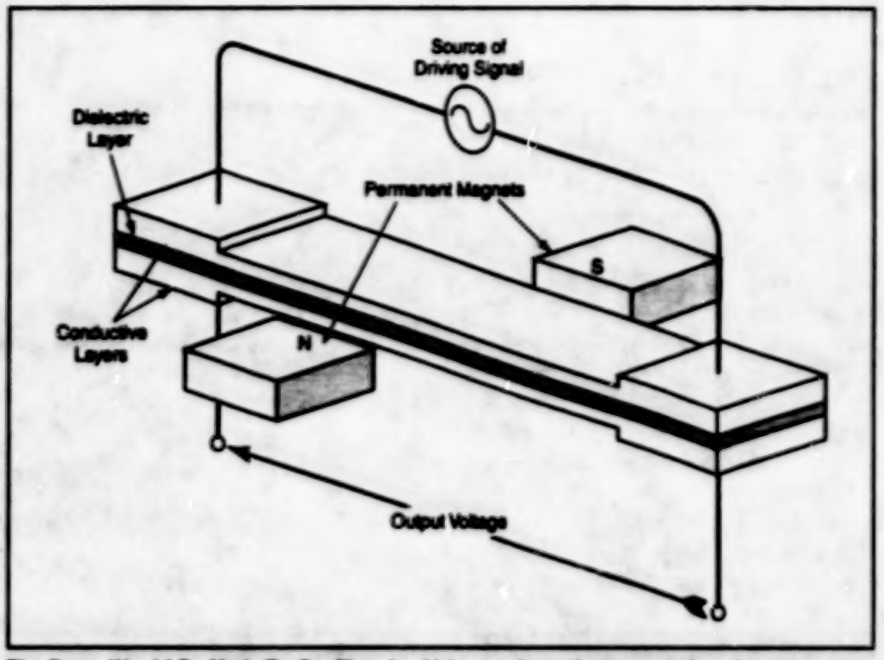

The Beam Would Be Made To Oscillate by driving an alternating current along the upper conductive layer in the presence of the permanent magnetic field. The oscillation would be measured by measuring the voltage induced in the lower conductive layer.

The smallness of the micromechanical oscillating mass balance would afford several distinct advantages over quartz-crystal microbalances and other related devices. The most obvious advantage is enhanced portability. The small size and mass of this device would also contribute to its ability to survive large vibrations and accelerations. Another important advantage pertains to thermal stabilization; smallness of size would minimize the effects of gradients of temperature, while smallness of mass would maximize the effectiveness with which the temperature of the device could be controlled. Temperature control could be accomplished easily by mounting this device directly on a Peltier device.

Another advantage would lie in relatively low cost associated with the relatively low driving frequency. Quartz-crystal microbalances operate at frequencies in the megahertz range, thereby requiring circuitry more expensive than that needed for operation in the kilohertz range. Yet another advantage would lie in the use of the fundamental mode of vibration of the beam. A theoretical analysis of the performance of a beam vibrating in its fundamental mode is easier than is the corresponding analysis for the quartz-crystal microbalance, which vibrates in a complex transverse mode.

This work was done by David Altemir of **Johnson Space Center**. *Further information is contained in a TSP [see page 1].*

This invention is owned by NASA, and a patent application has been filed. Inquiries concerning nonexclusive or exclusive license for its commercial development should be addressed to the Patent Counsel, Johnson Space Center [see page 1]. Refer to MSC-22569.

Polarization-Insensitive Electro-Optical Modulator Systems

Costs of light-wave communication systems could be reduced.

NASA's Jet Propulsion Laboratory, Pasadena, California

Electro-optical modulator systems of two proposed types would be insensitive to polarization; that is, variations in the polarization states of the input light waves to be modulated would not give rise to variations in the power levels of the output modulated beams. These modulator systems would be desirable in light-wave communication systems, including fiber-optic telephone, cable-television, and millimeter-wave communication systems, plus future personal mobile communication systems.

The commercial electro-optical modulators in current use are sensitive to polarization, making it necessary to take great care to ensure correct and stable polarizations in order to obtain stable outputs. This, in turn, necessitates the use of polarization-maintaining optical components — including, in many cases, polarization-maintaining optical fibers. In comparison with ordinary single-mode optical fibers, polarization-maintaining optical fibers cost about 20 times as much and are more difficult to handle; these characteristics contribute significantly to the high costs of present light-wave communication systems. Moreover, sensitivity to polarization precludes the use of single-mode optical fibers in the field, thereby inhibiting the establishment of the superior light-wave communication systems that could be built around electro-optical modulators. Because of their insensitivity to polarization, the proposed modulator systems would decrease the cost and increase the feasibility of such systems.

The upper part of the figure schematically illustrates a proposed polarization-insensitive modulator system of the first type. The incoming light wave to be modulated would first pass through a polarization beam splitter, which would decompose the beam into two beams in orthogonal polarization states. The two orthogonally polarized light waves would pass through separate electro-optical modulators driven by the same signal. The outputs of these modulators would be directed into a polarization beam combiner, where they would be recombined into a single output light wave.

The power of each polarization going into its respective modulator would depend on the angle of polarization, θ, of the input wave. However, the power of the output wave could be made independent of θ. Starting from the basic equations for the behavior of the various polarization components, it can be shown that if the two modulators were identical, then the power, P_{out}, of the output beam would be given by

$$P_{out} = \alpha P_{in}[\cos(\phi(V(t))+\phi_0)]^2,$$

where α is a transmission factor, P_{in} is the power of the input beam, $\phi(V(t))$ is the variation in phase angle as a function of the time-varying modulation voltage $V(t)$, t is time, and ϕ_0 is an initial phase determined by the bias voltage applied to the modulators.

The lower part of the figure illustrates a proposed polarization-insensitive modulator system of the second type. A polarization-independent beam splitter would split the incoming light into two parts of equal power and identical polarization states. One of these light waves would be directed along an optical path called the "reference arm," where it would travel directly to an output polarization-independent beam combiner. The other part would be directed along an optical path called the "signal arm," where it would be split further into orthogonally polarized waves that would be phase-modulated by the same signal, then recombined. Finally, the light from the reference and signal arms would be recombined in the output polarization-independent beam combiner. If the phase modulators in the signal arm were identical, then the output power would again be independent of θ and would be given by

$$P_{out} = (P_{in}/2)[\alpha_r+\alpha_s\cos(\phi_s(V(t))+\phi_{s0}-\phi_r)],$$

where α_r and α_s are transmission factors for the reference and signal arms, respectively; $\phi_s(V(t))$ is a modulation function like that described above, and ϕ_{s0} and ϕ_r are initial phase angles for the signal and reference arms, respectively.

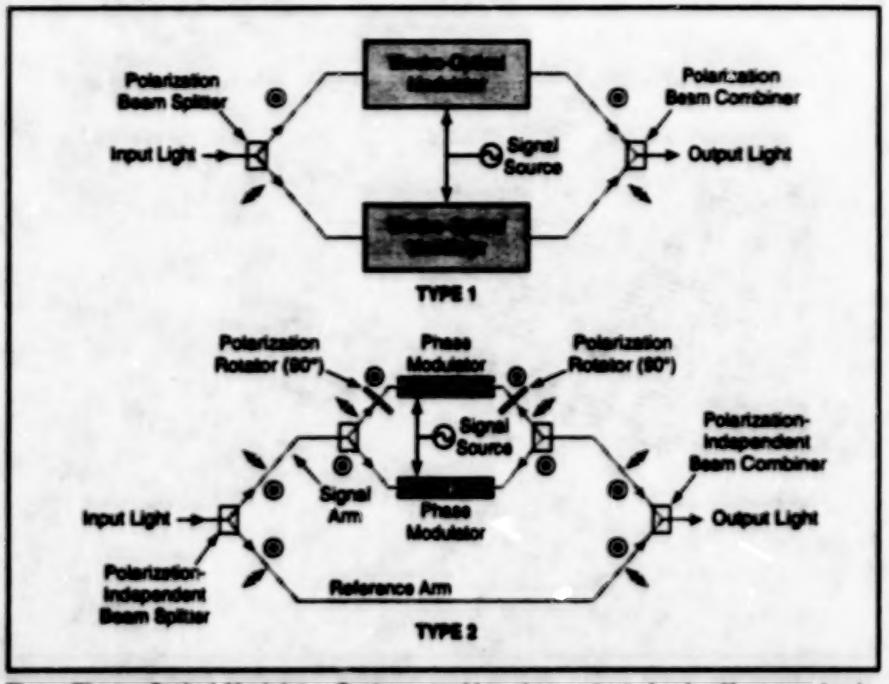

These Electro-Optical Modulator Systems would produce output signals with power levels independent of the polarization angles of the input light, provided that in each system, the modulators were identical.

This work was done by Xiaotien Steve Yao of Caltech for **NASA's Jet Propulsion Laboratory**. *Further information is contained in a TSP [see page 1].*

This invention is owned by NASA, and a patent application has been filed. Inquiries concerning nonexclusive or exclusive license for its commercial development should be addressed to the Patent Counsel, NASA Resident Office–JPL [see page 1]. Refer to NPO-19430.

One-Sided Focusing Schlieren System With Reflective Grid

All of the focusing optics are located on one side for compactness.

Ames Research Center, Moffett Field, California

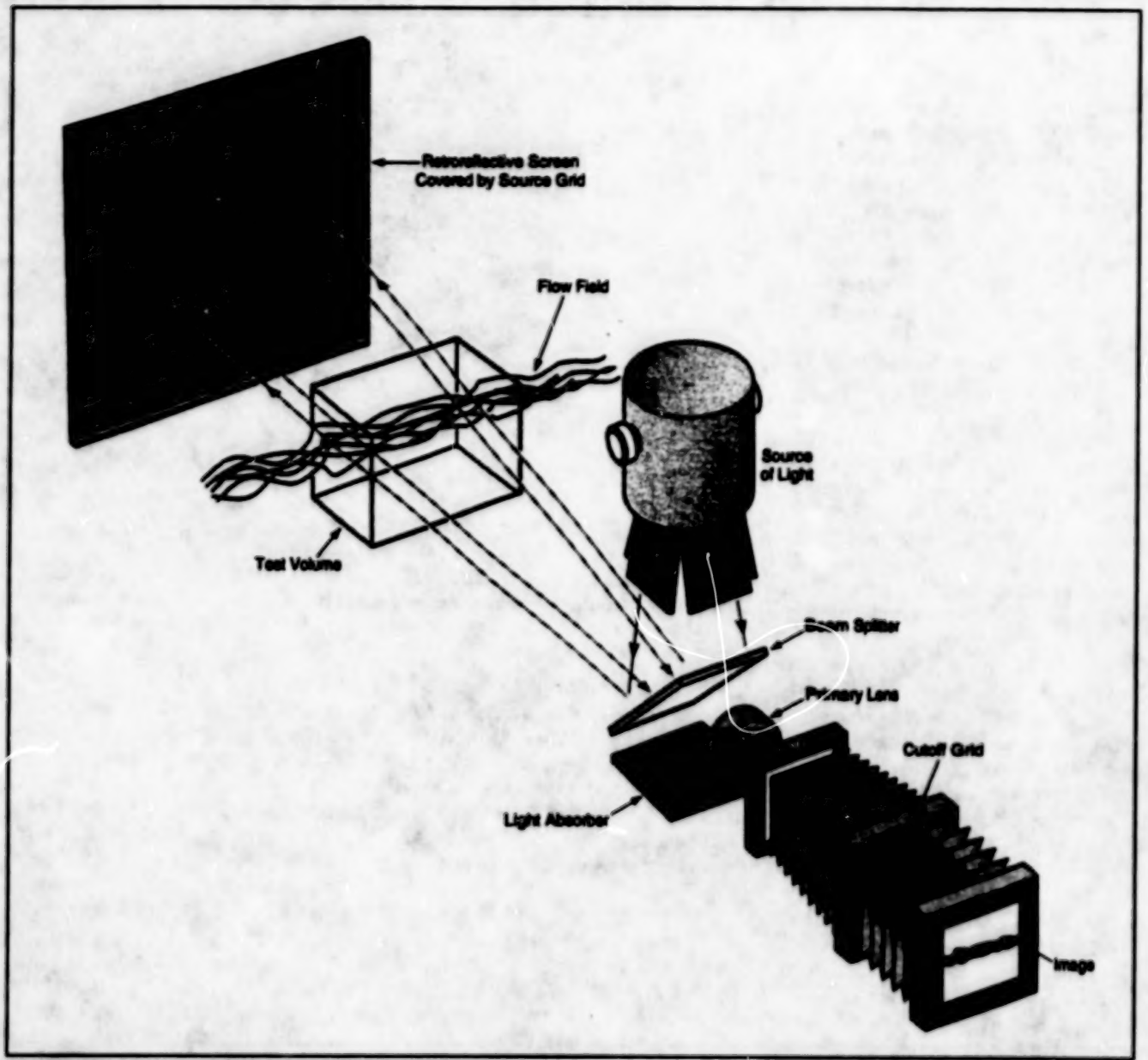

The Retroreflective Screen reflects light predominantly along the path of illumination through the source grid. The light passes through the flow field into the camera lens. Optionally, the beam splitter can be removed and the source of light can be placed alongside the camera and aimed parallel to the optical axis of the camera to illuminate the test volume and the retroreflective-screen/source-grid combination.

In an improved focusing schlieren system designed especially for observing flow in a wind tunnel, all of the focusing optics are located on one side of the volume to be observed (test volume), instead of on both sides as in older schlieren systems. Thus, most of the instrumentation can be mounted in a compact aerodynamic housing that perturbs the flow minimally and that can be positioned within the wind tunnel to obtain the required view of the observation volume.

The immediate predecessor to the improved system is a two-sided focusing schlieren system that utilizes grids instead of the knife edges of classical focusing schlieren systems. In the predecessor system, an illuminated Fresnel lens and frosted glass serve as a bright, diffuse source of light on one side of the test volume. A source grid lies between the Fresnel lens and the test volume. A camera located on the opposite side of the test volume faces the source grid, and a cutoff grid (the photographic negative of the source grid) interacts with the image of the source grid as modified by refraction in the test volume to provide the schlieren image. This image reveals gradients in the index of refraction and thus gradients of density in the flow in the test volume.

In the improved system, the source of light of the predecessor system is replaced by a screen of retroreflective material like that used in automobile license plates and road signs. The retroreflective material con-

tains prismatic particles that reflect light diffusely but with greatest intensity back along the path of arrival. A source grid is laid over the retroreflective screen. The grid-covered screen is mounted on one side of the test volume; it can be conveniently mounted on the wall or ceiling of the wind tunnel.

The other optical components of the system, including the cutoff grid, camera, and source of light, are mounted in an aerodynamic housing on the other side of the test volume (see figure). By use of a beam splitter, the source of light can be made to illuminate the screen and source grid along the optical axis of the camera. The retroreflective screen directs the light back along the same path through the source grid, and the schlieren image is formed in the same way as in the predecessor system. One side benefit of this arrangement is that instead of being silhouetted by back lighting as in older schlieren systems, objects in the test volume are illuminated from the camera side and, as a consequence, their details and interactions with the flow can be viewed more readily.

A tabletop model of the system was built to test its design. The model included an *f*/5.6 camera lens with a 300-mm focal length. The model exhibited a sensitivity of less than 9 arc seconds, which is comparable to that of a conventional schlieren system. The system had a depth of focus of less than 13 mm. A system of similar design was tested in the NASA Ames 7 × 10-ft (2.1 × 3-m) wind tunnel.

This work was done by James T. Heineck of **Ames Research Center** *and Stephen M. Jaeger of Sterling Federal Systems. Further information is contained in a TSP [see page 1].*

This invention has been patented by NASA (U.S. Patent No. 5,515,158). Inquiries concerning nonexclusive or exclusive license for its commercial development should be addressed to the Patent Counsel, Ames Research Center [see page 1]. Refer to ARC-13391.

First-Order Modeling of a Radiometer in Mathcad

The model can be adapted to almost any design requirements.

Stennis Space Center, Mississippi

A first-order mathematical model of an infrared radiometer functioning as a temperature sensor has been created within the Mathcad software framework. The model is a useful computational tool for designing and analyzing the performances of radiometers. The model provides easy access to the primary design parameters of a radiometer and enables the user to manipulate conditions to fit a wide range of applications.

In the model, the target (the object, the temperature of which one seeks to measure) is assumed to radiate according to Planck's radiation law as a gray body of known emissivity. The target is assumed to fill the field of view of the radiometer. The detector in the radiometer is assumed to be a thermopile with a response that is spectrally flat and linear with input (this linearity is known to be only an approximation). Other simplifying assumptions (involving various degrees of approximation) include that no correction for ambient temperature is necessary, that the spectral transmittance of the intervening atmosphere and the radiometer optics are uniform over all wavelengths, that there is no reflected radiation and no atmospheric or other radiance coming from sources other than the target, and that for purposes of computing the integral of spectral response of the radiometer over all wavelengths, the pass band of the radiometer can be represented by a trapezoidal response-vs.-wavelength plot.

The transmittance of the intervening atmosphere and radiometer optics are specified by the user. In the model, these parameters are lumped into one transmittance value, which is multiplied by the gray-body spectral radiance for a given target temperature and integrated over the pass band (which can also be specified by the user) to obtain the radiance at the detector. The response (output voltage) of the detector to this radiance is estimated from the detector specifications.

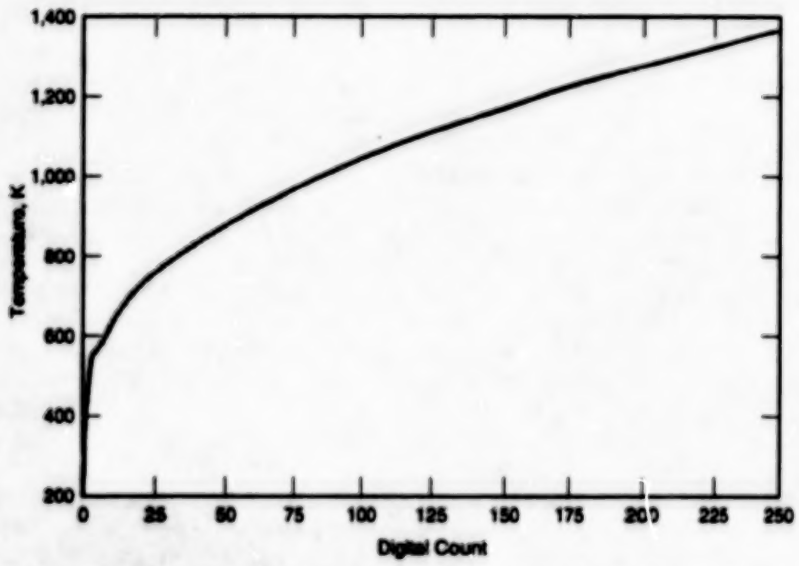

Temperature vs. Digital Count was computed for the lookup table in a test case.

The output of the detector is assumed to be fed through an amplifier to an analog-to-digital converter (ADC), the output of which is used to address an electronic memory that implements a lookup table of temperature vs. digital count (see figure). The model computes the amplifier gain needed to maximize resolution for the case of an 8-bit ADC with an input-potential span of 5 V. The model further computes the digital counts for the highest and lowest expected levels of radiance. The combination of counts and radiance is used to obtain a linear system transfer equation, which, in turn, is used to compute the count-to-temperature lookup table.

The Mathcad software framework makes it possible to relax some of the simplifying assumptions by incorporating the applicable spectral transmittances, reflectances, detector parameters, and/or other detailed information as needed. Thus, the model can be adapted to a more rigorous analysis to satisfy almost any design requirements. The model was created in Mathcad version 3.1 for UNIX, and can be implemented in any Mathcad version 3.0 or later.

This work was done by Bruce A. Spiering of **Stennis Space Center**. *Further information is contained in a TSP [see page 1].*

Inquiries concerning rights for the commercial use of this invention should be addressed to the NASA/SSC Technology Transfer Office, (601) 688-2346. Refer to SSC-00043.

Identifying Electric-Charge Locations With Potential To Generate Lightning

Locations and magnitudes of charges are computed from electric-field measurements.

John F. Kennedy Space Center, Florida

The Thunderstorm Localization Workstation (TLW) is a prototype of computers that would be dedicated to predicting the locations of imminent lightning strikes within geographical regions of the order of tens of kilometers. The TLW operates at a station that receives readings from electric-field sensors, called "field mills," at 31 ground locations in an array that spans Kennedy Space Center and Cape Canaveral Air Station. The signals are enhanced by use of advanced signal-processing techniques, then inverted by use of a mathematical model of the electric field to obtain the locations and strengths of thunderstorm electrostatic-charge centers from which lightning could emanate.

The TLW software is based partly on the Multiple Signal Characterization (MUSIC) algorithm, which is an eigenanalysis algorithm that has been used in tracking radio transmitters. In the present application, MUSIC is adapted to detect airborne electric charge centers.

The present adapted version of MUSIC incorporates both point-charge and dipole models of an electric field above a flat conductive ground. Usually, the point-charge model suffices to represent thunderstorm charge centers. Inasmuch as the field mills measure vertical electric fields, the point-charge model is formulated to express the vertical electric field (E) at each ground location of interest: $E = 2QD/(4\pi\varepsilon_0 r^3)$, where D is the altitude of the charge, Q is the amount of charge, ε_0 is the permittivity of the vacuum, and r is the distance from the charge to the ground location.

In preparation for predicting locations of lightning strikes, one defines a horizontal and vertical grid over the region of interest. A typical grid extends 10 by 20 by 10 km and has intervals of 1 km in all three dimensions. One then precomputes a transfer matrix, each element of which consists of $2D/(4\pi\varepsilon_0 r^3)$ for a given grid point and a given field-mill location. In the case of the 2,000-point grid described above and the Kennedy Space Center array of 31 field-mill locations, the transfer matrix contains $2{,}000 \times 31 = 62{,}000$ elements. Precomputation of the transfer matrix saves computing time, helping to make it possible to perform all other prediction computations in real time.

In the first two steps of the process, the TLW software reads data streams from the sensors and decimates the streams to a reasonable rate (typically between 1 and 10 samples per second) that is sufficient for tracking charge centers yet low enough to not contribute excessively to processing time. In the third step, the data are divided into segments between lightning strikes, segments that do not contain sensor- or field-saturation effects, and segments that do not contain sensor faults. A neural-network method is used to provide sensor-fault-detection capability beyond the capability provided by field-mill self-monitoring.

The fourth step is to determine the order of the mathematical model (in effect, the number of charge centers) on the basis of inspection of the eigenvalues of the selected segment. The fifth step is to perform the MUSIC inversion: The grid is scanned and at each point, a comparison is made between the eigenvectors of the selected segment and the eigenvectors of the transfer matrix. Good alignment between the two indicates that a charge center has been detected. The resulting three-dimensional function is called the "MUSIC spectrum."

The sixth step is to locate peaks of MUSIC spectrum by use of a peak-detector run over the spectrum. This run yields the three-dimensional coordinates of the charge centers.

The seventh step is to find the amounts of the charges by inserting the coordinates of the charge centers in the model and finding the least-squares best fit of the modeled electric field to the field-mill data. In the eighth step, the MUSIC spectrum and the location and charge information are presented in a display that resembles a weather map overlaid on a weather-radar image. In tests with field-mill and lightning-detection data from thunderstorms of recent years, the TLW charge-detection output data were found to agree with the lightning-detection data.

A method of optimizing the placement of the field mills has been developed along with the TLW. This method involves the use of Cramer-Rao bounds, and can be used to design field-mill arrays for other geographic areas. Cramer-Rao analysis has also shown that sometimes a vertical-dipole model performs better than the single-point model described above. Thus, it would be desirable to develop a computational method of distinguishing between single-point and dipole charges. Investigations using neural nets for localization and wavelets for signal segmentation show promise as future areas of research.

This work was done by Chris Berthold, Timothy M. Rynne, Kim J. Olszewski, and John T. Robinson of Scientific Applications & Research Associates, Inc., for Kennedy Space Center. Further information is contained in a TSP [see page 1].

In accordance with Public Law 96-517, the contractor has elected to retain title to this invention. Inquiries concerning rights for its commercial use should be addressed to

John T. Robinson
Scientific Applications & Research Associates, Inc.
15262 Pipeline Lane
Huntington Beach, CA 92649
(714) 373-5509

Refer to KSC-11859, volume and number of this NASA Tech Briefs *issue, and the page number.*

Light-Scattering Measurements of Regression of Fuel Droplets

The measurement principle is that of diameter-dependent resonance scattering from spheres.

Marshall Space Flight Center, Alabama

A proposed optoelectronic instrument would exploit the diameter-dependent resonance scattering of laser light from transparent spheres to measure the regression of liquid fuel droplets in spray flames. As used here, "regression" denotes a decrease, caused by evaporation, in the diameter of a droplet. The proposed instrument could be integrated with (a) a laser Doppler velocimeter for measuring the velocities of droplets; (b) a phase Doppler interferometer for measur-

ing the sizes of droplets; and (c) a rainbow refractometer for measuring temperatures of droplets and obtaining additional information about their sizes.

A description of rainbow phenomena is prerequisite to an explanation of the proposed instrument. The commonly recognized aspects of a rainbow can be understood in terms of a geometrical-optics-based theory proposed by Descartes several hundred years ago. The angular location of the primary rainbow arc for a given wavelength (called simply the "rainbow angle") can be understood to correspond to that scattering angle at which intensity of first-order internally reflected rays achieves a local maximum. To one side of the rainbow angle is a shadow region into which no rays emerge and to the other side is a lit region that contains additional rainbow arcs, called "supernumerary arcs," which are interference fringes that cannot be understood in terms of geometrical optics.

A point of light that is part of a supernumerary arc can be understood as arising from interference between two different rays of the same order emerging in the same direction. Thus, at any given scattering angle slightly greater than the rainbow angle, the scattered light includes rays that have followed two different paths through a droplet. To further complicate the situation, the interference of the internally reflected rays with externally reflected rays gives rise to high-frequency intensity oscillations that are superimposed upon the supernumerary arcs. These oscillations are extremely sensitive to small changes in the diameters of droplets. The proposed instrument is based on the proposition that these oscillations can be measured and, with suitable processing, data on changes in the diameters of regressing fuel droplets can be extracted from the measurements.

The extraction of droplet-regression data could proceed according to either or both of two approaches called the "phase" approach (for determining small changes in the sizes of drops) and "frequency" approach (for determining the rates of regression of drops). In the phase approach, the rainbow signature of a regressing droplet would be recorded at two known, closely separated instants of time. The recorded rainbow signatures would then be digitally processed to extract only the high-frequency contributions, and the two high-frequency signals would be correlated to extract the difference between their phases. This phase difference, ($\Delta\phi$) would be a measure of the change in the diameter of the droplet (ΔD) according to

$$\Delta\phi/\Delta D = d\phi/dD = (2\pi/\lambda)[\cos\theta_0 - \cos\theta_2 + 2m\cos(\sin^{-1}(\sin\theta_2/m))],$$

where ϕ is the instantaneous phase of the high-frequency signal at the rainbow angle, D is the instantaneous diameter of the droplet, λ is the wavelength of the scattered light, θ_0 and θ_2 are the angles of incidence of light on the droplet that give rise, respectively, to the externally and internally reflected rays that emerge at the rainbow angle, and m is the index of refraction of the droplet at wavelength λ.

In the frequency approach, the intensity of scattered light would be monitored by a photodetector through a very small aperture located at the rainbow angle. As the droplet regressed, the intensity would oscillate at a frequency equal to the rate of regression multiplied by the expression on the right side of the equation above. The validity and feasibility of both the phase and frequency approaches have been demonstrated in experiments in which a "breadboard" prototype of the instrument was used to observe both nonburning and burning droplets made by a piezoelectric droplet generator.

This work was done by Subramanian V. Sankar, Dale H. Buermann, and William D. Bachalo of Aerometrics, Inc., for **Marshall Space Flight Center**. *Further information is contained in a TSP [see page 1].*

Inquiries concerning rights for the commercial use of this invention should be addressed to the Patent Counsel, Marshall Space Flight Center [see page 1]. Refer to MFS-26402.

BLANK PAGE

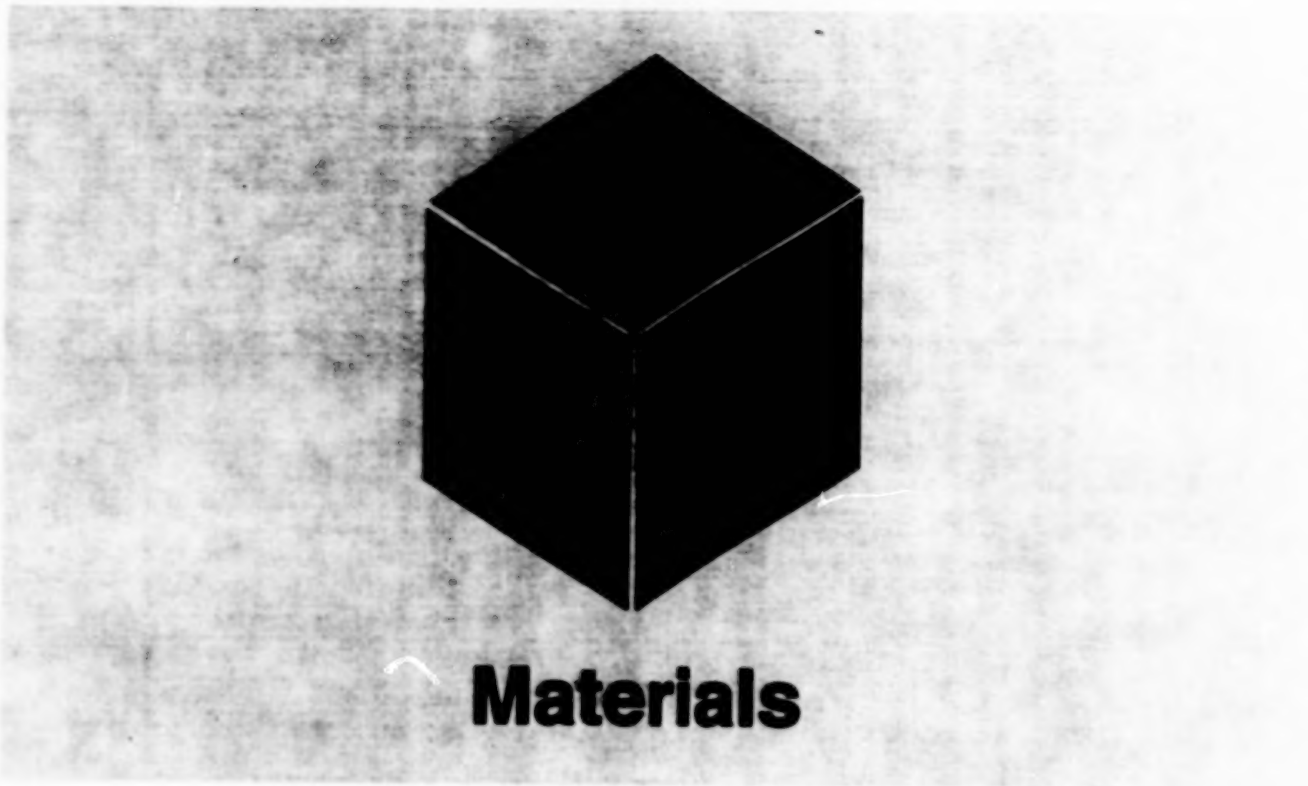

Materials

Hardware, Techniques, and Processes

37 Making InP Solar Cells From Tertiarybutylphosphine
37 Monolithic Foam Supports for Iridium Catalysts
38 Heteroepitaxial Growth of Monocrystalline Boron Nitride

BLANK PAGE

Making InP Solar Cells From Tertiarybutylphosphine

The risk of exposure to toxic fumes is reduced substantially.

Lewis Research Center, Cleveland, Ohio

Experiments have shown that tertiarybutylphosphine (TBP) is suitable for replacing phosphine as a precursor chemical in the fabrication of indium phosphide-based solar photovoltaic cells. Heretofore, doped and undoped films of InP for solar cells have been grown by organometallic vapor-phase epitaxy (OMVPE), using phosphine (PH_3) and trimethylindium [$In(CH_3)_3$] as precursor chemicals. Excellent InP films can be formed from these precursors, but phosphine must be supplied in excess for the OMVPE chemical reactions and is extremely toxic; its threshold limit value (TLV) is 0.3 parts per million and it is lethal in concentrations as small as several parts per million. The potential for a substantial hazard arising from leakage of an industrial quantity of phosphine could well inhibit mass production of InP.

TBP was selected as a candidate to replace phosphine because it is much less toxic (TLV 1,100 parts per million). TBP is supplied as a liquid, the vapor pressure of which is suitable for introduction into an OMVPE reactor. TBP costs more than phosphine does, but the greater cost of TBP would be offset by the reduction of risk and simplification of treatment of effluent from the OMVPE process. Prior to these experiments, excellent InP films for microwave semiconductors had been grown with TBP at concentrations smaller than the corresponding concentrations of phosphine, and at temperatures lower than those used for phosphine. However, prior to these experiments, InP films with areas large enough and minority-carrier lifetimes long enough for efficient solar cells had not been grown from TBP.

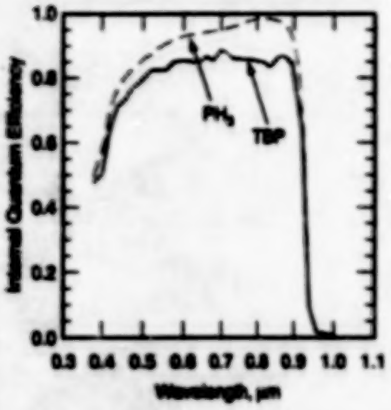

	TBP	PH_3
FF%	82.6	82.4
V_{oc} (mV)	871	876
J_{sc} (mA/cm²)	30.7	35.3
p+ Buffer	No	Yes
Dual Layer ARC	No	Yes

Internal Quantum Efficiency was among the parameters measured in tests of cells made with TBP and compared with values from cells made with PH_3. The slight deficit of the TBP cell with respect to the PH_3 cell in this example is attributed to defects that were present in the substrate of the TBP cell prior to epitaxial deposition of InP from TBP. Presumably, such defects could be eliminated in future units.

In the experiments, doped and undoped InP films were deposited from TBP and $In(CH_3)_3$ precursors injected into a flow of purified hydrogen, which served as a carrier gas. The gas pressure in the reactor was typically 150 torr (20 kPa). The deposition substrate was heated to a temperature of 590 °C. Acceptor (p) doping was achieved by injection of diethyl zinc into the flow of H_2; donor (n) doping was achieved similarly, using silane as the precursor. Some of the films were used to fabricate solar cells, which were then tested. The tests showed that in most respects, the cells made with TBP performed comparably (see figure) to state-of-the-art cells made with phosphine.

In the table, the measured solar-cell performance parameters of open circuit voltage V_{oc}, short-circuit current density J_{sc}, and fill factor FF for the TBP cell are compared to performance data from the world record PH_3-produced InP solar cell. The only shortfall of the TBP cell is in J_{sc}, which can be improved to comparable levels by minor adjustments to the device structure. The internal quantum-efficiency data only show the short-circuit current deficiency of the TBP cell compared to the PH_3 cell.

This work was done by David M. Wilt, David J. Brinker, and William E. Frey of Lewis Research Center, Richard W. Hoffman, Jr., of Analex Corp., and Navid S. Fatemi, Phillip P. Jenkins, and David A. Scheiman of NYMA, Inc. Further information is contained in a TSP [see page 1].

Inquiries concerning rights for the commercial use of this invention should be addressed to the Patent Counsel, Lewis Research Center [see page 1]. Refer to LEW-16314.

Monolithic Foam Supports for Iridium Catalysts

Experiments indicate that monolithic catalysts can outperform granular catalysts.

Lyndon B. Johnson Space Center, Houston, Texas

Experiments have demonstrated the feasibility of catalytic beds in the form of iridium (the active catalytic material) supported by monolithic foams composed of noncatalytic materials. Heretofore, the state-of-the-art commercial iridium catalyst has consisted of iridium supported on alumina spheres.

The monolithic foams can be made of materials that withstand temperatures of 2,000 °C or more. In comparison with catalytic beds made of packed iridium-coated granules, the developmental foam-supported catalysts offer greater catalytic surface area with less weight, present less resistance to the flow of reactant gases, and do not degrade over time with regard to performance or flow resistance. In addition, the foam-supported catalysts can be made to exhibit lower thermal masses and lower thermal conductivities so that they absorb less heat from reactants. This is an important advantage if the application is as a catalytic igniter in a liquid-propellant rocket engine, with fuel/oxidizer reactant combinations such as hydrogen/oxygen (H_2/O_2) or monomethyl hydrazine/nitrogen tetroxide (MMH/NTO).

Some of the supporting materials under consideration are special high-surface-area carbon foams made, in part, by augmentation of precursor materials and subsequent processing to obtain the desired porosity. Iridium is then formed on the surfaces of the foam ligaments. Other promising foam materials include silicon carbide, silicon nitride, boron carbide, titanium boride, and hafnium carbide, although the experiments performed thus far indi-

cate that carbon is the most effective foam material over a wide range of flow conditions (depending on the materials being catalyzed). Further development efforts are expected to focus on optimization of fabrication processes to maximize surface areas, levels of catalytic activity, operating temperatures, and life expectancies and to improve thermomechanical properties and environmental compatibility.

This work was done by Raffaele La Ferla, Qin Jang, Robert H. Tuffias, and Richard B. Kaplan of ULTRAMET for **Johnson Space Center**. *Further information is contained in a TSP [see page 1].*
MSC-22287

Heteroepitaxial Growth of Monocrystalline Boron Nitride

Thin films of b-SiC would be used as substrates for deposition of cBN.

NASA's Jet Propulsion Laboratory, Pasadena, California

In a proposed deposition process, monocrystalline cubic boron nitride (cBN) would be grown heteroepitaxially on silicon carbide films. Success in the development of the process would enable the growth of bulk cBN (perhaps also diamond) for making high-temperature, high-power, high-frequency electronic devices.

Heretofore, the growth of monocrystalline boron nitride heteroepitaxial layers has been impeded by the lack of a suitable substrate material; to obtain the monocrystalline form, one must use a substrate with a crystalline lattice that closely approximates that of cBN. When silicon and other substrate materials have been tried, the lattice mismatches have resulted in amorphous BN in some cases and polycrystalline BN in other cases.

The substrate material in the proposed process would be a film of β-SiC, 10 to 30 μm thick. The film would be formed on a substrate of single-crystal silicon, then removed from the silicon substrate and mounted in a graphite holder that would minimize bowing. The film, mounted in the holder, would be placed in an electron-cyclotron-resonance chemical-vapor-deposition chamber, where BN would be grown on the film. The lattice mismatch between the film would give rise to a compressive stress in the film, causing the film to bow slightly. The slight yielding of the film under the lattice-mismatch stress would reduce the lattice mismatch enough to allow the BN to grow in the desired cubic-lattice monocrystalline form.

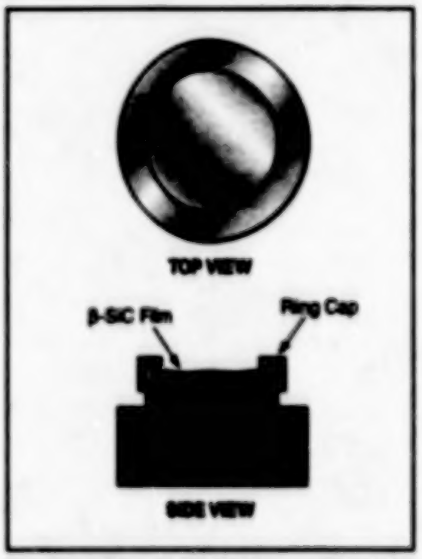

The Ring Cap on the Holder would help to minimize bowing of the β-SiC film during chemical vapor deposition of BN.

This work was done by Virgil B. Shields and Frederick Pool of Caltech for **NASA's Jet Propulsion Laboratory**. *Further information is contained in a TSP [see page 1].*
NPO-19761

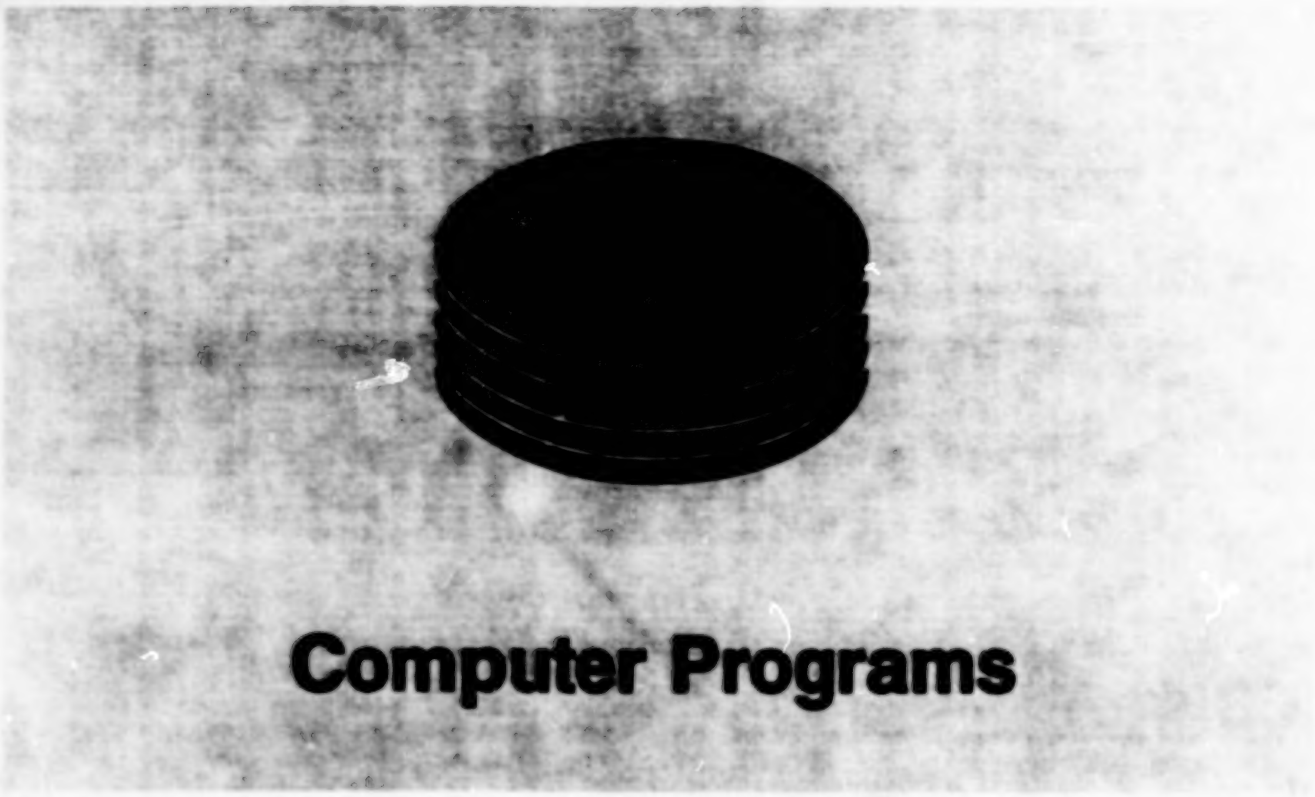

Computer Programs

Physical Sciences

41 Software Restores Image Blurred By Spatially Variable PSF
41 Program Generates Point-Spread Functions

Mathematics and Information Sciences

41 Software for Efficient Dynamic Management of Memory Space

BLANK PAGE

These programs may be obtained from COSMIC. Please contact

COSMIC®
Computer Services Annex
University of Georgia
Athens, GA 30602
Telephone No. (404) 542-3265.

Physical Sciences

Software Restores Image Blurred By Spatially Variable PSF

The Massively Parallel Richardson-Lucy (MPRL) computer program implements the Richardson-Lucy algorithm, which deconvolves an image from a spatially variant point-spread function (SV-PSF). MPRL was developed to restore blurred images produced by the Hubble Space Telescope, but is also applicable to other optical systems in which images are sensed by charge-coupled devices or other arrays of discrete photodetectors. Because deconvolution is computationally intensive and SV-PSF deconvolution more so, the use of parallel (concurrent) processing techniques greatly accelerates the code throughput. This entails much more computation than is needed for deconvolution with a spatially invariant PSF in the Fourier domain, making it desirable to accelerate the computation by use of parallel (concurrent) processing. In the Richardson-Lucy algorithm, concurrency is achieved by systematic division of the image to be restored. Only pixel values within the support of the PSF are interdependent; thus, an arbitrary division of the image into segments with appropriate overlapping guard bands enables the independent processing of each segment. In MPRL, such concurrency is realized by use of a public-domain library known as the Parallel Virtual Machine (PVM) communications package. PVM makes it possible to implement a Richardson-Lucy restoration engine and to spawn a large number of such engines, each restoring different sections of the image, on a heterogeneous set of Unix workstations. MPRL is also portable to such computers as the Intel Paragon and the Cray T3D.

This program was written by Andrew F. Boden of Caltech for **NASA's Jet Propulsion Laboratory.** *Further information is contained in a TSP [see page 1].*
NPO-19914

Program Generates Point-Spread Functions

The Simulated Hubble Space Telescope (SHST) computer program generates point-spread functions (PSFs) to simulate the blurred images of stars and other point objects as they would appear in the Wide Field Planetary Camera II of the Hubble Space Telescope. The PSFs capture the imaging effects of diffraction and of imperfections in the telescope, camera optics, and camera photodetectors. SHST comprises an application program and sets of data, which include the prescription of the telescope, maps of imperfections of the telescope mirrors, and data on filters and other optical components. The application program uses the prescription and other data to trace a large grid of rays through the telescope and camera optics. The rays determine phases and vignetting for physical-optics calculations of diffracted images at the photodetectors. The images are resampled to the specified pixel size. This process is repeated for each spectral line to build up a particular PSF. The PSFs generated by SHST can be used in image-restoration programs — for example, the MPRL program described in the preceding article. SHST runs on Unix workstations like the Sun SPARC and DEC Alpha computers. The prescription files in SHST are compatible with the commercial MACOS optical-analysis application program, which was developed in part by NASA's Jet Propulsion Laboratory.

This program was written by David Redding of Caltech for **NASA's Jet Propulsion Laboratory.** *Further information is contained in a TSP [see page 1].*
NPO-19937

Mathematics and Information Sciences

Software for Efficient Dynamic Management of Memory Space

The Personal Space Management (PSM) computer program is a library of subprograms that provide functions to support efficient, dynamic partitioning of a contiguous block of random-access memory to suit an application program or programs. PSM minimizes processing overhead incurred in the management of memory space, minimizes waste of memory space, and prevents one application from using all memory space and thereby causing other applications to fail. PSM divides each partition of memory space into two "pools" of variable size; a "small" pool of low-overhead blocks containing as many as 256 bytes of user data apiece, and a "large" pool of high-overhead blocks that contain as many as 2GB of user data. The "small" pool provides extremely rapid management of the blocks within it, while the "large" pool manages its blocks somewhat less rapidly but makes a greater effort to minimize waste of space. PSM runs under either VxWorks or SunOS 4.1.3 on a variety of computers.

This program was written by Scott Burleigh of Caltech for **NASA's Jet Propulsion Laboratory.** *Further information is contained in a TSP [see page 1].*

This software is available for commercial licensing. Please contact Don Hart of the California Institute of Technology at (818) 393-3425. Refer to NPO-19903.

BLANK PAGE

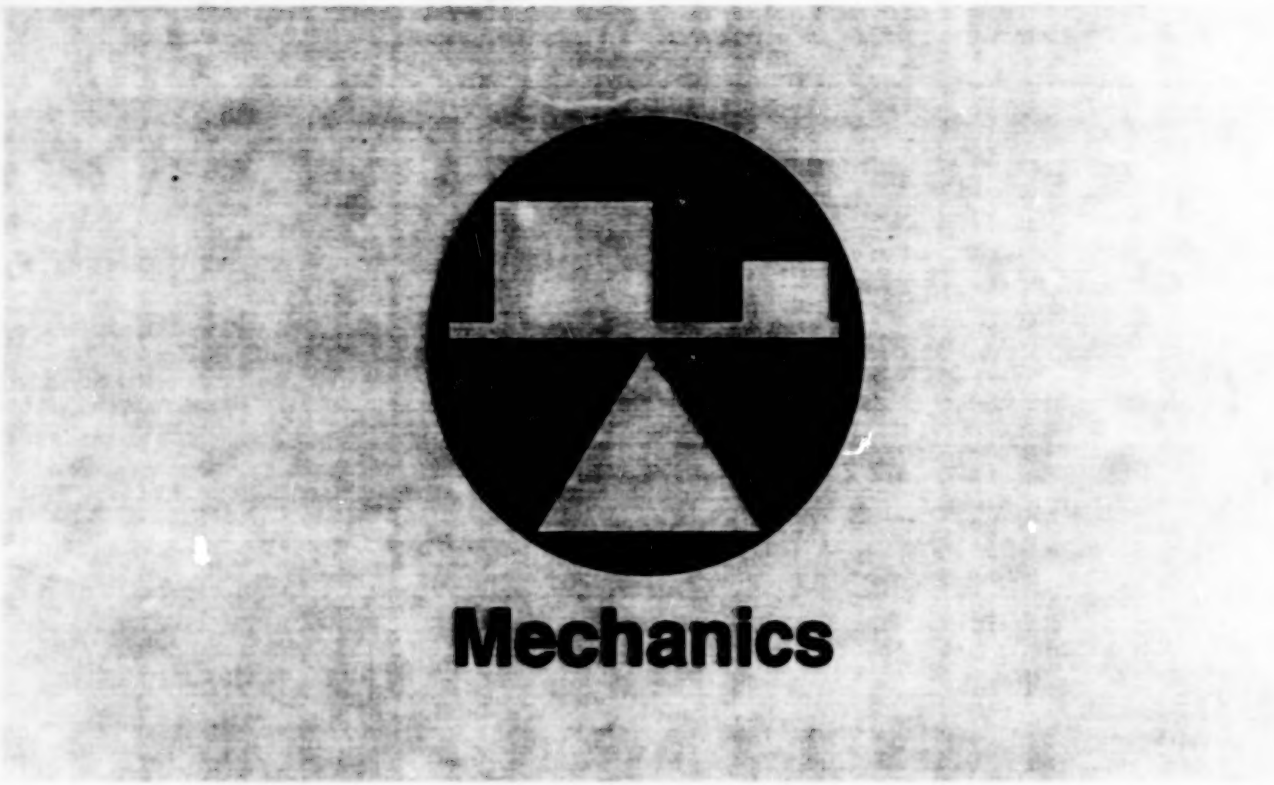

Mechanics

Hardware, Techniques, and Processes

45 Constructing Finite Elements for the Integrated Force Method
46 Optically Controlled Microvalves for Microfluidic Devices
47 Thermostatic Valve for Low-Pressure-Drop Flows of Gas
47 Improved Fillets To Withstand Thermal Shocks
48 Removable, Reusable Handle

BLANK PAGE

Constructing Finite Elements for the Integrated Force Method

These finite elements help to realize the potential of the integrated force method.

Lewis Research Center, Cleveland, Ohio

A method of constructing finite elements for use in two- and three-dimensional structural analysis by the integrated force method has been devised. In the integrated force method, all independent forces are treated as unknown variables that can be calculated on the basis of simultaneous imposition of equations of equilibrium and conditions of compatibility. Developed in recent years, the integrated force method offers advantages of greater accuracy and computational efficiency, relative to the standard displacement method.

The two-dimensional finite elements that can be constructed by the present method are triangular and quadrilateral elements (see Figure 1) that can be used in modeling arbitrary configurations. The three-dimensional finite elements that can be constructed by this method include tetrahedrons and hexahedrons analogous to the triangular and quadrilateral two-dimensional elements, plus tetrahedron- and hexahedron-like volumes with curved edges (see Figure 2).

The mathematical derivation for two dimensions begins with the construction of equilibrium and flexibility matrices for the elements from discretized equations for potential and complementary energies, respectively. The displacement and stress fields within the finite elements are independently approximated. The displacement field is interpolated in the same way as in the standard displacement method.

The stress field is approximated by complete polynomials of the correct order. The coefficients of these polynomials are initially unknown independent forces. The equations that describe the components of the stress tensor can be derived from the Airy stress function for an element, which is written in terms of a complete polynomial of a certain order. The resulting stress field identically satisfies the equations of equilibrium. The element matrices generated by use of this stress field are not sensitive to the orientation of the local coordinate system of the element.

The method includes a way of calculating the number of zero-energy (rigid-body) modes. It turns out that spurious zero-energy modes can be eliminated by constructing the stress field such that for each element, $n_i \geq n_s - 1$, where n_i is the rank of

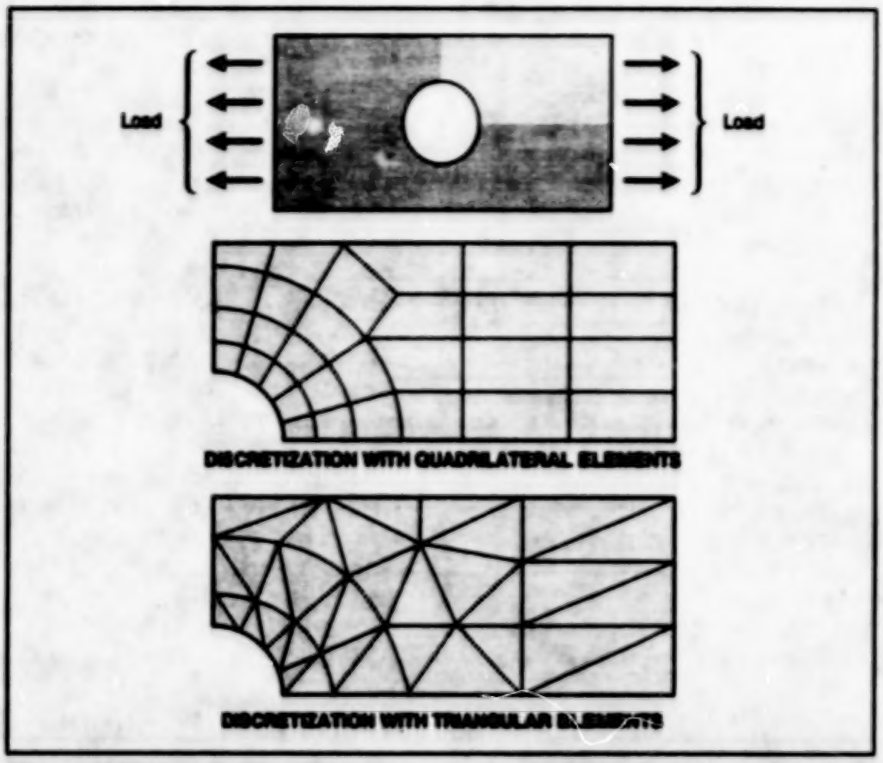

Figure 1. A Rectangular Plate With a Round Hole in uniform tension is one of many structural-analysis problems that can be solved by the integrated force method, using triangular or quadrilateral finite elements generated by the method described in the text.

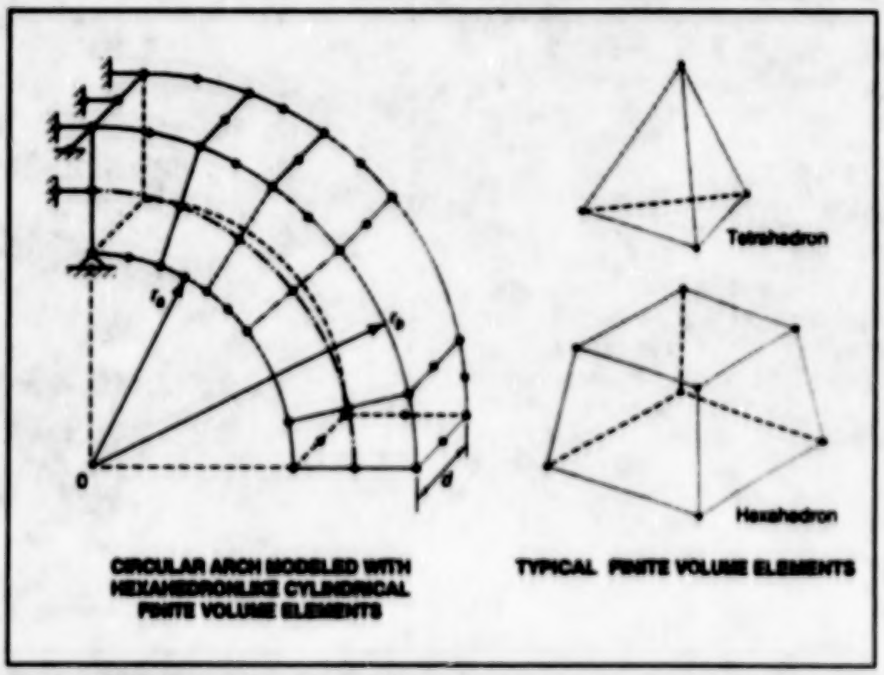

Figure 2. Tetrahedral, Hexahedral, and Similar Elements can be used to model bodies with arbitrary shapes. For example, a circular arch can be modeled by concatenated hexahedron-like cylindrical volume elements of axial length *d*, inner radius r_o, and outer radius r_i.

the equilibrium matrix of the element and n_e is the number of kinematic degrees of freedom of the element.

The mathematical derivation for three dimensions resembles that for two dimensions in some respects. It begins with a general formulation to generate a stress-interpolation matrix for each finite volume element terms of complete polynomials of the required order. The formulation is based on definitions of components of the stress tensor in terms of stress functions. The stress functions are expressed as complete polynomials and substituted into equations for stress components. Then elimination of linearly dependent coefficients leaves the stress components expressed as complete polynomials, the coefficients of which are defined as generalized independent forces. The components of the stress tensor thus derived identically satisfy the homogenous Navier equations of equilibrium. The resulting element matrices are invariant with respect to coordinate transformations and are free of spurious rigid-body modes.

The formulation provides a rational way to calculate the exact number of independent forces necessary to arrive at a complete-polynomial approximation of the required order. Unfortunately, interpolation of stress with complete polynomials can necessitate the use of a large number of independent forces for each element, in some cases leading to inconveniently large final systems of equations. Therefore, it could be worthwhile to attempt to reduce the number of independent forces in stress-interpolation polynomials while preserving the accuracy and reliability of the resulting finite elements. However, one should proceed with caution because at present, there is no rational procedure for uniquely deriving stress fields with minimum numbers of independent forces, there is no proof that the resulting elements are free of spurious zero-energy modes, and in some problems, the elements can fail unexpectedly.

The present method has been tested on two- and three-dimensional example stress-analysis problems for which exact solutions are available. In the tests, the problems were solved by (1) the integrated force method using finite elements generated by the present method and (2) the standard displacement finite-element method. In the two-dimensional tests, it was found that overall, the integrated force method using finite elements generated by the present method performed better than did the standard displacement method in predicting stresses, and that the integrated force and displacement methods performed comparably in predicting displacements. In the three-dimensional tests, it was found that typically, the integrated force method using finite volume elements generated by the present method performed about as well as or better than did the standard displacement method in predicting stresses.

This work was done by Dale A. Hopkins of **Lewis Research Center** *and Igor Kaljevic and Surya N. Patnaik of Ohio Aerospace Institute. Further information is contained in a TSP [see page 1].*

Inquiries concerning rights for the commercial use of this invention should be addressed to NASA Lewis Research Center, Commercial Technology Office, Attn: Tech Brief Patent Status, Mail Stop 7–3, 21000 Brookpark Road, Cleveland, Ohio 44135. Refer to LEW-16421.

Optically Controlled Microvalves for Microfluidic Devices

These valves would be actuated remotely, without external electrical connections.

NASA's Jet Propulsion Laboratory, Pasadena, California

Optically controlled microvalves have been proposed for use in microfluidic devices. These microvalves would be actuated remotely via the photoactuation effect that occurs in the ferroelectric/piezoelectric material lead lanthanum zirconate titanate (PLZT).

Microvalves are needed in biomedical, microchemical, microirrigation, microspacecraft, and microavionics applications. With miniaturization, it becomes desirable to eliminate the extra baggage of peripheral electronic controls and umbilical cords that are customarily used in remotely controlling valves equipped with electrically driven actuators. The elimination of electrical connections is especially important where there is a need for electrical isolation for safety; for example, in biomedical applications that involve the delivery of insulin or the control of flows in artificial organs. Photoactuation is thus an attractive option for such applications.

The basic principle of photoactuation by use of PLZT was described in "Thin-Film, Light-Energized Bimorph Micromechanical Actuators" (NPO-19607), *NASA Tech Briefs*, Vol. 20, No. 8 (August 1996), page 11a. The actuator in a microvalve of the proposed type would be made largely of PLZT, which could be either free-standing or formed on a thin substrate of Si, Si_3N_4, or other suitable material. The figure shows a

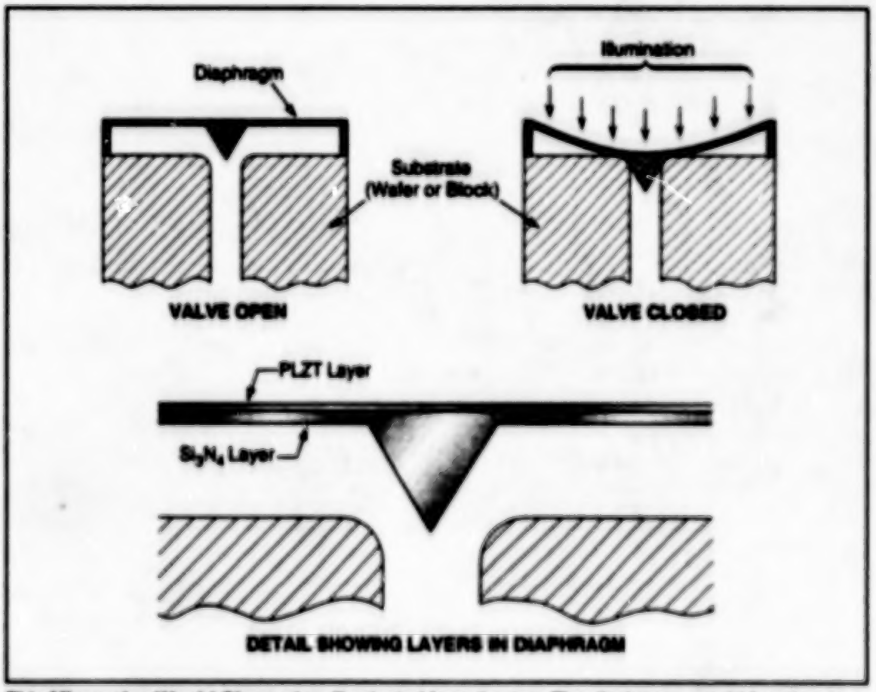

This Microvalve Would Close when illuminated from the top. The diaphragm would function as a photoactuator by virtue of the ferroelectric/piezoelectric effect in PLZT.

proposed microvalve actuated by a two-layer (PLZT/Si_3N_4) diaphragm. Incident light would cause the diaphragm to bend down in the middle, closing the valve; a similar microvalve could also be configured so that illumination would cause the valve to open. Such valves could be actuated by pulses of light to obtain pulses of flow and/or pressure in the fluids to be controlled.

The proposed microvalves would be made by micromachining techniques like those used to make very-large-scale integrated (VLSI) circuits, and could be embedded in VLSI wafers. They could be readily tailored to suit for specific applications. They could be produced in batches and could be inexpensive enough to be regarded as expendable.

This work was done by Sarita Thakoor and Terry Cole of Caltech for **NASA's Jet Propulsion Laboratory**. *Further information is contained in a TSP [see page 1].*
NPO-19661

Thermostatic Valve for Low-Pressure-Drop Flows of Gas

Hot and cold inlet flows are mixed to obtain intermediate temperature at the outlet.

John F. Kennedy Space Center, Florida

A thermostatic bypass diverter valve mixes hot and cold inlet flows of a gas to obtain an outlet flow at an approximately constant intermediate temperature. The valve (see figure) includes slotlike inlets and a flag mounted on a bimetallic strip. The flag can block either or both inlet(s) to various degrees, thereby altering the proportions of entering hot and cold flows. The degrees of blockage of the inlets depend on the bend of the bimetallic strip; this bend, in turn, depends on temperature.

The valve is intended for use in a system in which the pressure drops elsewhere along the relevant flow paths are low. It is anticipated that neither 100-percent cold flow nor 100-percent hot flow would ever be needed in this system. Therefore, leakage of either the hot or the cold flow through a nominally totally blocked inlet is not of concern, and the valve can be designed with generous clearances while still restricting the inlet flows enough to obtain the desired control. Large clearances can be utilized to reduce friction and drag, which could cause binding.

At the time of reporting the information for this article, the valve had not yet been tested for sensitivity to vibration. Should the valve prove sensitive to vibration in its operational environment, the mass of the flag and/or the bimetallic strip can be adjusted to avoid resonance, and/or the parts adjacent to the clearance gaps could be coated with polytetrafluoroethylene or a similar material to provide limited frictional damping.

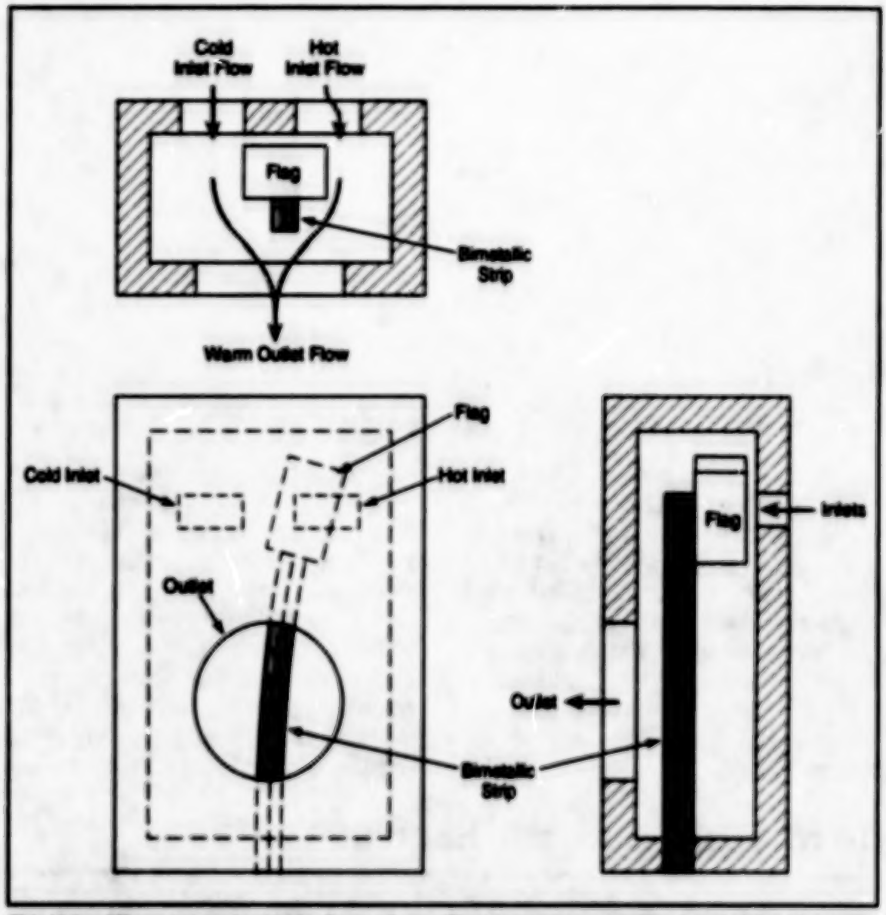

This Valve Mixes hot and cold inlet flows of gas. The temperature-sensitive bend of the bimetallic strip determines the mixing proportions and thus the temperature of the outlet flow.

This work was done by Paul F. Berg of United Technologies Corp. for **Kennedy Space Center**. *No further documentation is available.*

Inquiries concerning rights for the commercial use of this invention should be addressed to Patent Counsel, Kennedy Space Center [see page 1]. Refer to KSC-11871.

Improved Fillets To Withstand Thermal Shocks

Some material would be removed to reduce thermal gradients.

Marshall Space Flight Center, Alabama

Improved larger-radius fillets have been proposed to help some right-angle structural joints in turbine engines endure thermal shocks that occur during rapid heating and cooling. The joints in question could be, for example, those between turbine-vane airfoils and the endwalls that support the airfoils.

The problem of thermal shock (transient thermally induced mechanical stress) in joints of this type arises for the following reasons: It is well documented

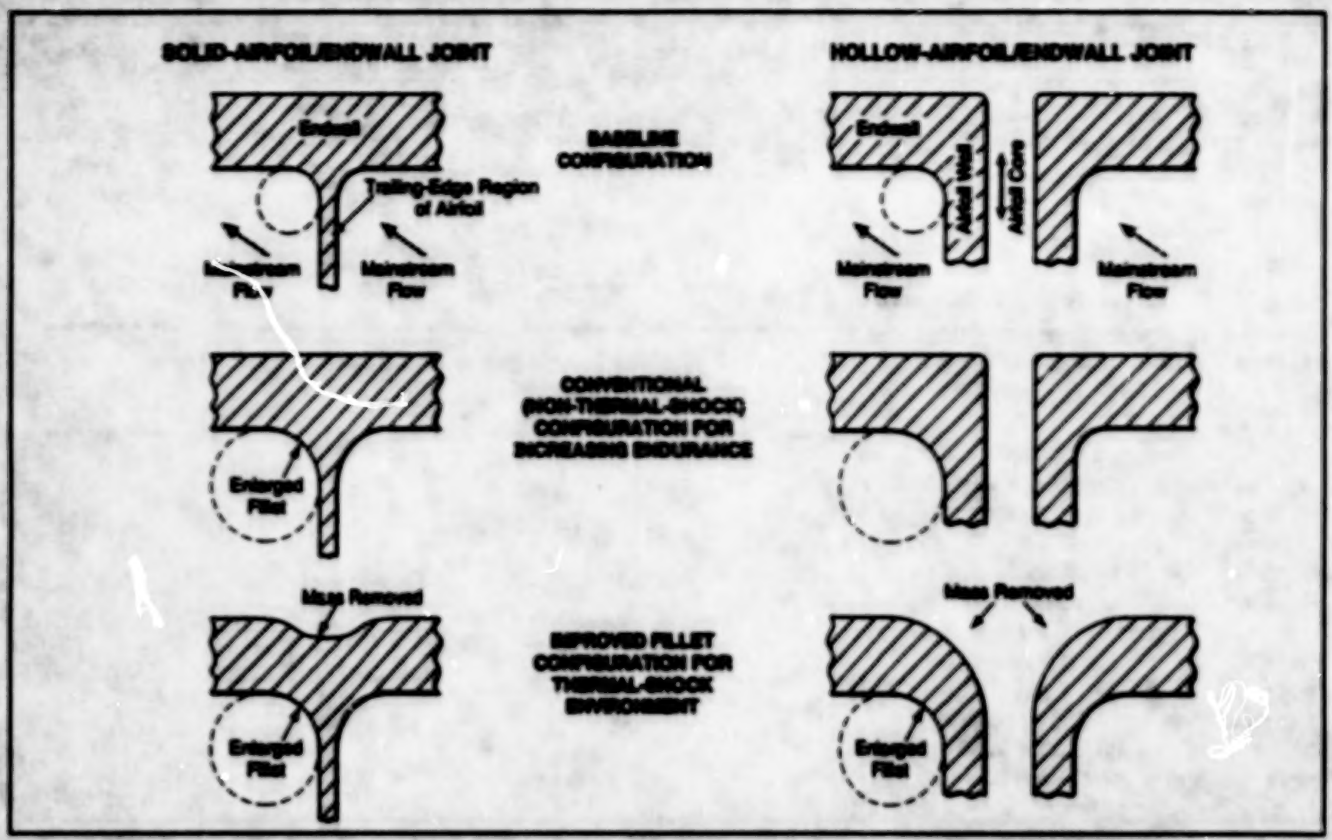

Removal of Mass from back sides opposite fillets would increase thermal-shock endurance by decreasing thermal gradients.

that in the absence of thermal transients, such a joint can be made more durable by increasing its fillet radius to reduce concentration of mechanical stresses. Unfortunately, in the presence of thermal transients, the mass added by increasing the fillet radius serves as a medium that supports increased local gradients of temperature; this causes thermal stresses to increase, negating the benefit of the larger fillet radius.

The figure shows representative solid- and hollow-airfoil/endwall joints in the baseline, conventional larger-fillet-radius (non-thermal-shock), and proposed larger-fillet-radius configurations. In the proposed configurations, the fillets would be enlarged to reduce concentration of stresses as in conventional practice. In addition, some mass would be removed from the back sides opposite the fillets. The removal of mass from the vicinity of the fillets would reduce thermal stresses by reducing the gradients between the typically higher temperatures along the sides of the airfoils and the typically lower mass-average temperatures of the fillet regions.

This work was done by Donald E. Paulus of United Technologies Pratt & Whitney for Marshall Space Flight Center. No further documentation is available.
MFS-28743

Removable, Reusable Handle

The handle can be attached and detached quickly and easily.

Lyndon B. Johnson Space Center, Houston, Texas

HANDLE SEPARATED FROM BASEPLATE

HANDLE PLACED ON BASEPLATE BUT NOT TURNED INTO LOCKING POSITION

HANDLE IN LOCKING POSITION ON BASEPLATE

The Installation or Removal of the Handle involves both rotation and pushing a button — the lock button for installation and the release button for removal. Rotation is clockwise for installation, counterclockwise for removal.

A detachable handle fits specially designed modular equipment cabinets. There is no need to provide each cabinet with its own handle; weight is thus saved and a streamlined cabinet surface is preserved. The handle can be installed and removed with only one hand. It can be used quickly, its state is unambiguous, and its operation is reliable.

The handle mates with a baseplate that is bolted to a face of a cabinet. A human or robotic operator first inserts a stub that protrudes from the handle into a positioning receptacle on the baseplate, then turns the handle 30° clockwise, so that interlocking conical surfaces of the stub and receptacle slide into contact. The operator pushes a locking button within the reach of a thumb on the handgrip rail on the handle. This action causes a pin to protrude from the stub into a hole in the receptacle in the baseplate, thereby locking the handle to the baseplate and cabinet.

To remove the handle, the operator pushes a releasing button near the baseplate. The releasing button is placed far enough from the locking button that the releasing button is unlikely to be pushed accidentally. The operator rotates the handle 90° counterclockwise and can then extract the handle from the baseplate. Even if the release button were pushed inadvertently, the handle would still have to be rotated 90° to be released fully. Inasmuch as only one of the two buttons can protrude at any time, the user can easily see the state of locking.

This work was done by Robert P. Nespodzany, Jr., of Honeywell, Inc., for **Johnson Space Center**. *Further information is contained in a TSP [see page 1].*

Title to this invention has been waived under the provisions of the National Aeronautics and Space Act [42 U.S.C. 2457(f)], to Honeywell, Inc. Inquiries concerning licenses for its commercial development should be addressed to

Mr. Ron Champion
Honeywell, Inc.
Satellite System Operations
PO Box 52199
Phoenix, AZ 85072-2199
(602) 436-1980

Refer to MSC-22126, volume and number of this NASA Tech Briefs *issue, and the page number.*

BLANK PAGE

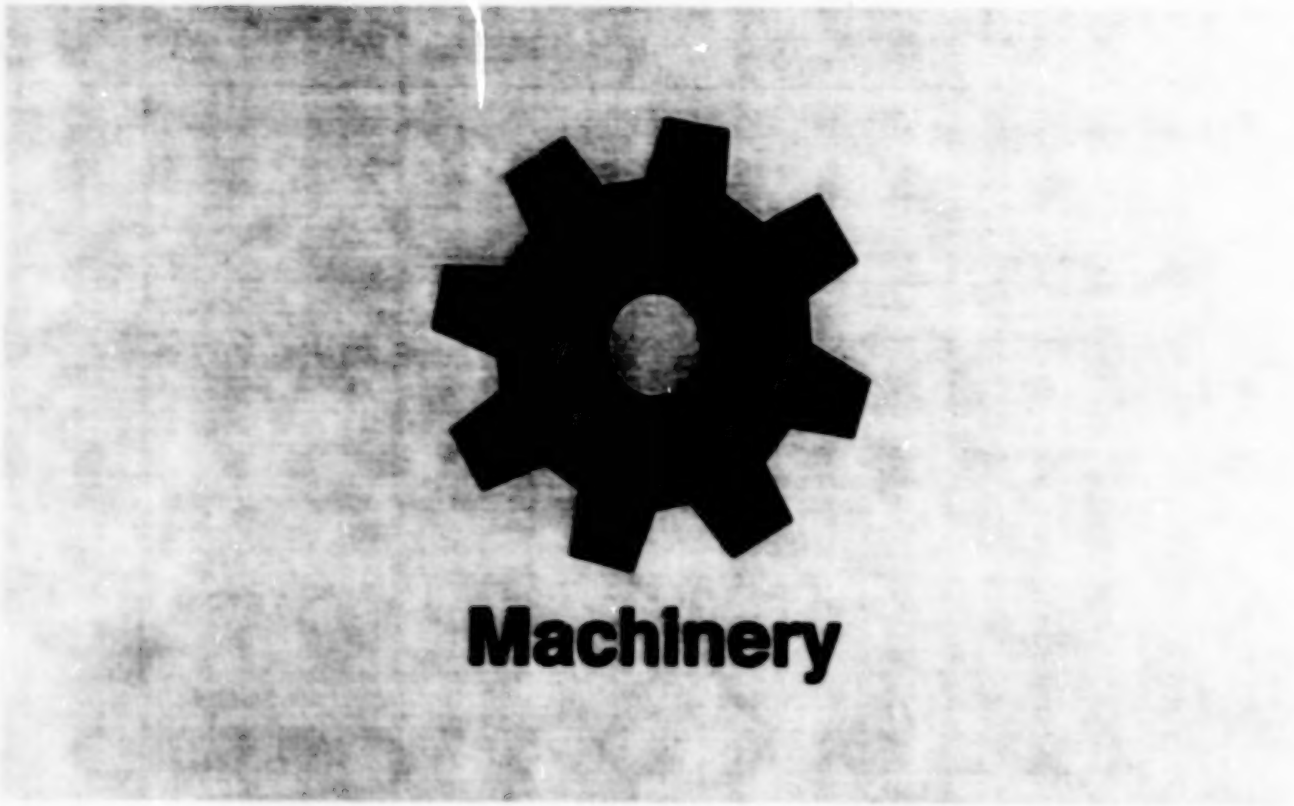

Machinery

Hardware, Techniques, and Processes

53 First Supersonic Yaw-Vectoring Flight for the ACTIVE Program

BLANK PAGE

First Supersonic Yaw-Vectoring Flight for the ACTIVE Program

Yaw is controlled via thrust vectoring.

Dryden Flight Research Center, Edwards, California

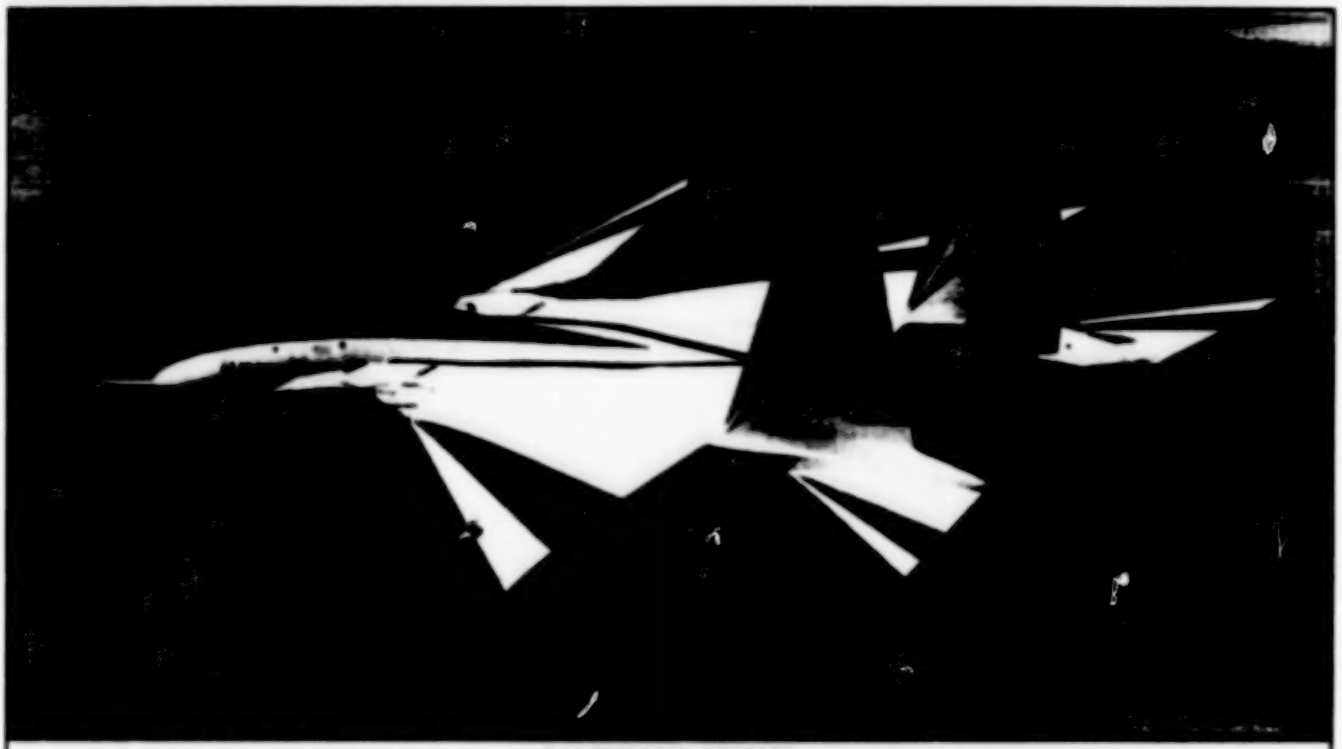

F-15 RESEARCH AIRCRAFT

- Fail-safe design accommodates flight condition: nozzle remains open in supersonic flight, closes once flight becomes subsonic.
- Pin joints (no roller tracks or sliders) maximize resistance to wear.
- Divergent design enables independent exhaust-area control with optimal scheduling for performance and acoustics.

Photo courtesy of Pratt & Whitney

ENGINE WITH THRUST-VECTORING NOZZLE

The ACTIVE F-15 Aircraft features two state-of-the-art engines modified to include multidirectional thrust-vectoring nozzles.

The F-15 Advanced Control Technology for Integrated Vehicles (ACTIVE) aircraft recently engaged in its first supersonic yaw-vectoring flight at Dryden Flight Research Center. ACTIVE is a joint program of NASA, the U.S. Air Force, McDonnell Douglas Aerospace, and Pratt & Whitney. The ACTIVE team will expand the flight envelope of the aircraft engine nozzles to mach 2 and 750 KCAS (knots calibrated airspeed) with maximum vector angles, rates, and power settings. In addition, the team will assess performance benefits and identify aerodynamic effects induced by two vectored supersonic jet exhausts. Current plans call for approximately 60 flights with a total time of 100 hours.

The F-15 research aircraft used in the ACTIVE program (see figure) is a one-of-a-kind system. For the first yaw-vectoring flight, power to reach supersonic speeds was provided by two state-of-the-art F100-PW-229 engines modified by installation of a pair of pitch/yaw balance beam nozzles (P/YBBNs), which are multidirectional thrust-vectoring nozzles that were used to vector the engine thrust horizontally and vertically during the flight.

For NASA's flight research, each P/YBBN was mounted on one of the two engines. The fan-duct cases of the engines were modified to provide the additional strength needed to withstand the vectoring forces. Installation of the P/YBBNs also necessitated minor modifications of the rear fuselage and main engine mounts. The P/YBBNs are symmetrical and can direct thrust at an angle up to 20° with respect to the engine centerline. The balanced-beam concept, which has been proven in service in F100 convergent/divergent exhaust nozzles, minimizes control actuation loads and reduces the need for heavy, reinforced structures.

Each P/YBBN nozzle includes a fail-safe dual redundant actuation system, making it compatible with single-engine as well as twin-engine aircraft. The PW-229 engine with a similar pitch/yaw-vectoring nozzle has been selected for integration into a modified F-16D aircraft in

the U.S. Air Force's Variable-Stability In-flight Simulator Test Aircraft (VISTA) program. Moreover, the P/YBBN has been selected for the concept demonstrator Joint Strike Fighter competition aircraft.

Benefits expected to accrue from thrust vectoring in future aircraft include extended range, increased maneuverability, reduced operating cost, and greater safety. The present thrust-vectoring concept should lead to significant increases in performance of both civil and military aircraft flying at subsonic and supersonic speeds. Another important feature is the production-oriented P/YBBN design, which will ease transition of vectoring technology to production applications.

This work was done by Gerard Schkolnik, Tim Conners, John Orme, Bob Sims, Mike Earls, Kevin Kellenberger, John Carter, Mark Stephenson, Ting Tseng, and Karla Shy of **Dryden Flight Research Center**, *Jim Disbrow, Wes Ryan, and Mike Muratore of Analytical Services & Materials, Pete Schaefer of Sparta, and Michael Hultano, Don Warren, and John Flynn of McDonnell Douglas Aerospace. Further information is contained in a TSP [see page 1].*

DRC-96006

Fabrication Technology

Hardware, Techniques, and Processes

57 A_{2J} X-Ray Grids on Si by Optical Lithography and Etching

57 Collimating Cylindrical Microlens Assembly for Diode-Laser Arrays

BLANK PAGE

Au X-Ray Grids on Si by Optical Lithography and Etching

These grids can be used in an x-ray solar telescope.

NASA's Jet Propulsion Laboratory, Pasadena, California

Fine-pitch, thin gold grids supported by silicon substrates have been developed for use in pairs to collimate x rays in imaging and spectroscopic instruments. These grids are designed to provide collimation at photon energies up to 30 keV. A representative grid of this type (see figure) comprises gold x-ray-absorbing slats 25 μm thick and 17 μm wide, with a pitch of 34 μm (so that the slats and the slits between them are of equal width). The grid also includes integral stiffeners perpendicular to the slats, with a pitch of 500 μm. The grid occupies an area 5.5 cm in diameter on the silicon substrate, which is a 200-μm-thick wafer of 3-in. (7.62-cm) diameter.

The silicon substrate is semitransparent at photon energies >10 keV, but blocks x rays with photon energies as low as 2 keV. To prevent the substrate from blocking the passage of low-energy x rays and to enable optical characterization of the grid, the silicon substrate is perforated with holes 1 mm wide by 4 mm long with rounded ends. These holes are arranged in staggered rows with their long axes perpendicular to the slits and slats.

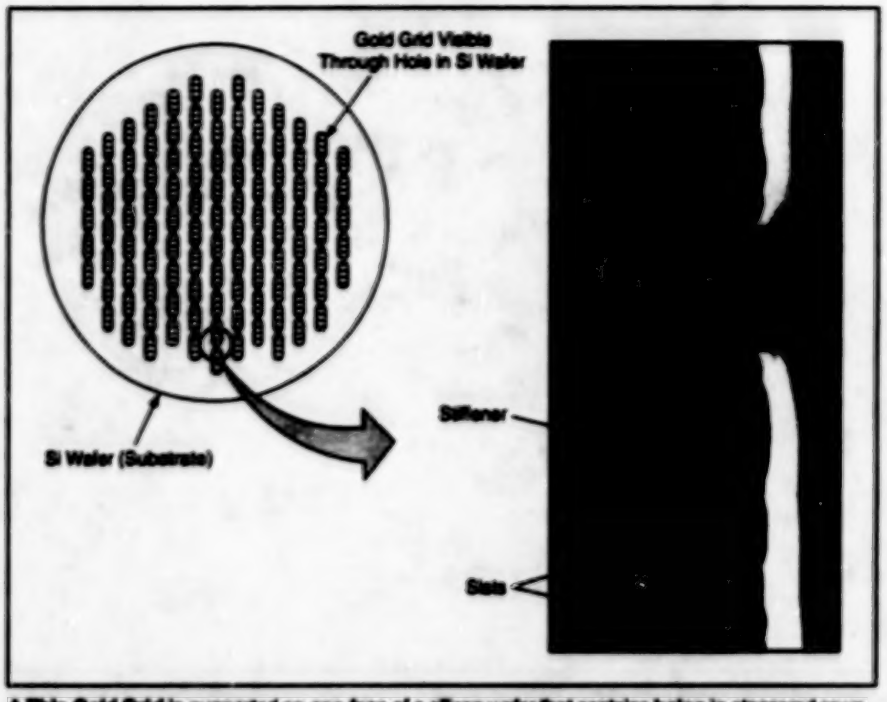

A Thin Gold Grid is supported on one face of a silicon wafer that contains holes in staggered rows. The holes allow lower-energy x rays to pass through the wafer to the grid, and enable optical inspection of the grid.

Fabrication of the grid begins with evaporative deposition of a 50-Å-thick layer of Cr followed by a 300-Å-thick layer of Au on one side of the substrate to form a seed coat ("strike") for subsequent electroplating of the 25-μm-thick layer from which the grid will be made. A photoresist 25 μm thick is deposited on the strike, exposed in the grid-and-stiffener pattern, and developed. An oxygen plasma is used to strip resist residue from the strike. Then gold is electrodeposited onto the exposed parts of the strike between the remaining photoresist ridges to a thickness of 25 μm, forming a gold grid with photoresist between the slats.

The wafer is turned over and a 50-μm dry resist is applied and exposed in the pattern of the holes to be formed through the substrate. Using equipment at UC Los Angeles, the exposed parts of the substrate are etched through the entire thickness of the substrate by use of XeF_2 gas, which reacts with silicon to generate gaseous products that are carried away by a vacuum pump. The remaining parts of both photoresists are then removed by use of acetone followed by a "piranha" bath (5:1 H_2SO_4:H_2O_2). The Cr/Au strike in the holes through the substrate is removed by use of a solution of 3:1 HCl:H_2O_2, which etches Cr much more rapidly than it etches Au. Finally, a ring made of a low-thermal-expansion nickel/iron alloy (Invar or equivalent) is glued to the wafer.

Prototype grids fabricated in this way have been characterized by use of a visible-light calibration system to verify the registration of the grids. The grids were found to satisfy the registration specifications to the limit of the calibration system. The gold grids have been shown to be usable for the collimation purpose for which they were designed and can be easily tested by laser techniques while they are mounted in place in scientific instruments.

This work was done by Reid A. Brennen, Dean V. Wiberg, and Michael H. Hecht of Caltech and David Pankow of The Space Sciences Laboratory, UC Berkeley, for **NASA's Jet Propulsion Laboratory.** *Further information is contained in a TSP [see page 1].*

NPO-19857

Collimating Cylindrical Microlens Assembly for Diode-Laser Arrays

Lasers are used to define lens axes via photolithography.

Goddard Space Flight Center, Greenbelt, Maryland

A method of fabrication of cylindrical microlenses in precise alignment with two-dimensional arrays of diode lasers has been invented. The method is applicable to arrays in which the light-emitting facets of the individual lasers are typically about 10 μm wide and 1 μm high. These are etched in a semiconductor chip, which is cut into 1-cm wide chips, or bars, for mounting in two-dimensional stacks, as shown in Figure 1. The interbar spacing is typically 400 μm, which is the minimum spacing in which the heat can be removed effectively from each chip. These packages are assembled and soldered manually, thus the interbar spacing can vary by ± 40 μm. The light emitted from these facets is highly divergent in the cross-sectional plane

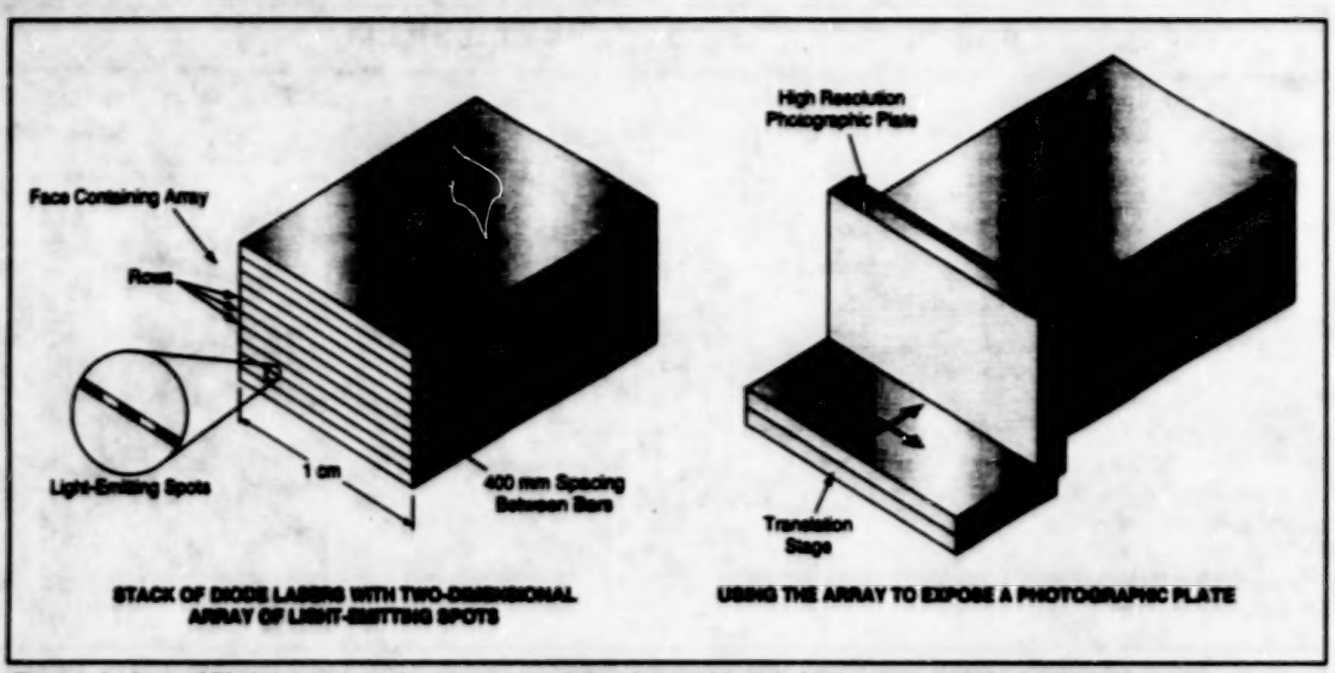
Face Containing Array
Rows
Light-Emitting Spots
1 cm
400 mm Spacing Between Bars
STACK OF DIODE LASERS WITH TWO-DIMENSIONAL ARRAY OF LIGHT-EMITTING SPOTS
High Resolution Photographic Plate
Translation Stage
USING THE ARRAY TO EXPOSE A PHOTOGRAPHIC PLATE

Figure 1. An Array of Diode Lasers is used to expose a translating photographic plate, forming streak images coincident with its rows.

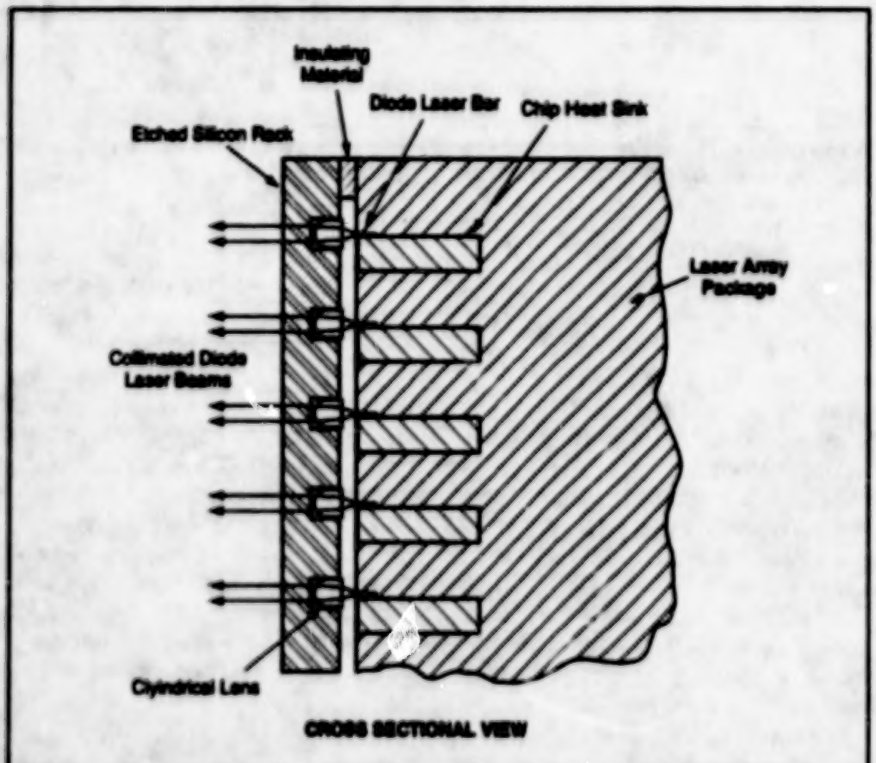

Figure 2 A Fully Assembled Lens Rack and a Diode Array are shown here. Strips or a layer of insulating material (e.g., tape), or high-temperature epoxy can be applied to the remaining flat face of the plate to set the lens-to-laser distance accurately for collimation.

perpendicular to the rows, due to diffractive effects of the 1-μm aperture. Precisely aligned cylindrical lenses are needed to collimate each 1-cm row of beams for efficient coupling to external devices; for example, coupling pump light into solid-state laser crystals. The assembly of cylindrical lenses for a two-dimensional stack of arrays is very difficult, as each lens placement requires micron accuracy.

The essence of the method is to use the pattern of light emitted by a diode-laser array as the master pattern to define a pattern of cylindrical lens placement on a rack that can later be registered mechanically with the array. First, a sheet or plate of photolithographic film is placed on a translational stage, parallel to the face of the array. The plate is placed in contact with the diode array. (This does not damage the semiconductor material, as each chip is mounted on individual heat-sink shims, recessed by around 40 μm from the front of the array package.) The array is turned on to expose the plate, making a 1:1 image of the individual rows of diode lasers. The photographic film is then gently pulled away from the array and translated a few millimeters to the left or right and reset in contact with the array where another laser pulse is exposed on the film. When performed correctly and with the correct intensity, a 12- to 14-mm wide image is formed from which a chrome-on-glass photomask can be made for photolithography. Of course, all the handling of the film and the exposing process must be performed in darkness. To reduce the difficulty of making exposures, a laser "camera" has been constructed that allows the complete alignment and setting up of the laser array and film to be done in low light. All that is left for the darkness is the removal of the exposure plate and the adjustment of the laser array to contact the film.

The photomask is used for the standard photolithographic process where a silicon wafer is etched with troughs, corresponding with the exact arrangement of the particular diode array. The trough aspect ratio and wall slope angle are determined by (1) the photoresist ultraviolet exposure and etching times and (2) the orientation of the silicon crystal lattice in the wafer, respectively. A central section of the etched image, corresponding to the emitting face

dimensions of the diode-array package, is cut from the silicon wafer. What remains is a rectangular hole with etched troughs, a few millimeters wide, on opposing sides of the hole. It is in these troughs that the ends of tiny cylindrical lenses will be precision glued into place, such that the lenses will span the hole and be identically spaced with each other as the individual bars in the laser-diode array. The cylindrical lenses are silica rods, 100 to 300 μm in thickness, and are drawn into shape like fiber optics. Through this process, an ashperical shape can be produced on the front and the back of the lens, thus creating an excellent single-element optic (see Figure 2).

This work was done by D. Barry Coyle of **Goddard Space Flight Center**. *Further information is contained in a TSP [see page 1], or e-mail: barry@eb1.gsfc.nasa.gov.*

This invention is owned by NASA, and a patent application has been filed. Inquiries concerning nonexclusive or exclusive license for its commercial development should be addressed to the Patent Counsel, Goddard Space Flight Center [see page 1]. Refer to GSC-13635.

BLANK PAGE

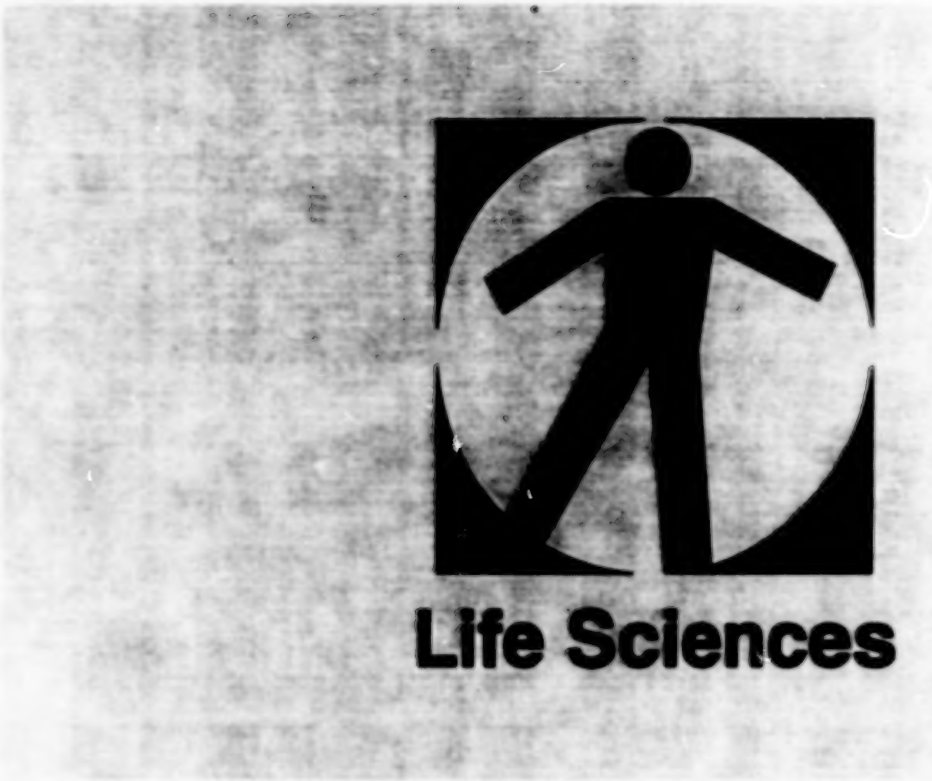

Life Sciences

Hardware, Techniques, and Processes

63 Automated Microspectrofluorimeter and Cell-Culture Apparatus

64 Microwave Treatment of Cardiac Arrhythmias

BLANK PAGE

Automated Microspectrofluorimeter and Cell-Culture Apparatus

Outstanding attributes include compactness, frequency agility, and computer control.

John F. Kennedy Space Center, Florida

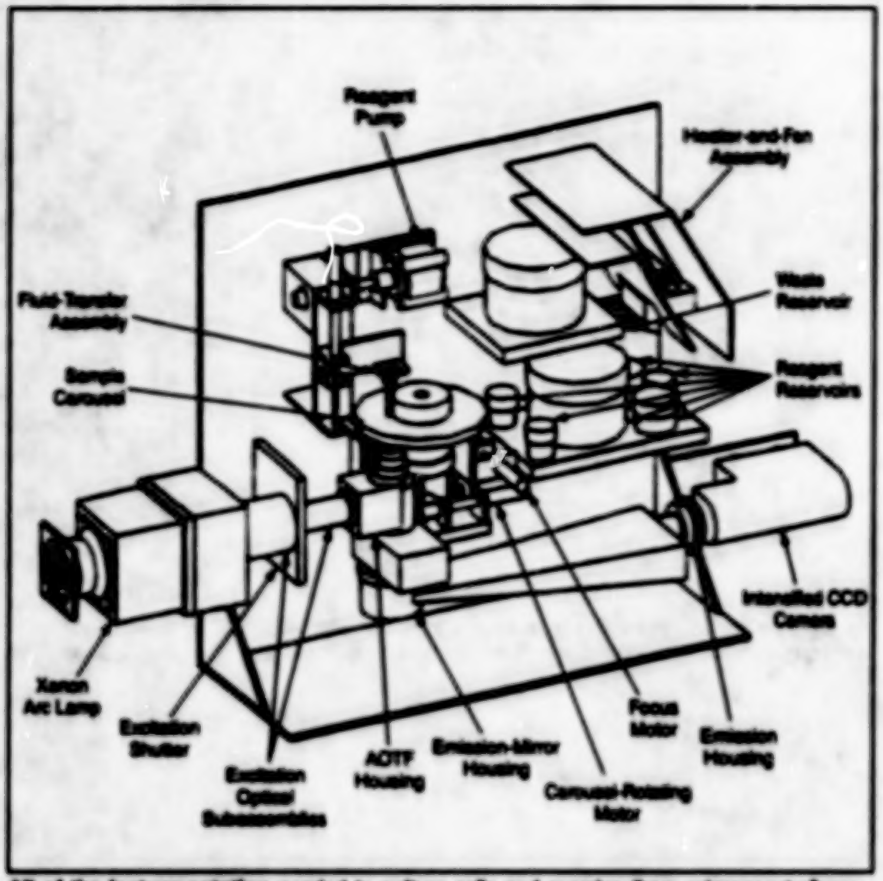

All of the instrumentation needed to culture cells and examine them microspectrofluorometrically is contained in one compact package.

A developmental compact instrument for experimentation on live cells includes a cell-culture-and-imaging module plus a frequency-agile microspectrofluorimeter for examining the cells. The cell-culture-and-imaging module not only maintains cell cultures but also provides for the necessary transfers of substances to change nutrient media and to stimulate, fix, and label cultured cells. The microspectrofluorimeter provides tunable, multiple-wavelength visible light to illuminate the specimens; acquires quantitative, spectrally-resolved images of single cells; digitally processes the images; and stores the resulting data.

The instrument is designed to operate under computer control; it can be programmed to perform a variety of functions and left to operate unattended after initial loading with cells, culture media, stimulatory chemicals, inhibitory chemicals, and/or other materials. Originally intended for use aboard a spacecraft, the instrument also offers advantages for terrestrial laboratory and field experimentation and clinical investigations: Its automation, programmability, and frequency agility could prove beneficial in such applications as cytometry and pathological examinations of biopsy specimens.

Of all the innovations incorporated into the design of the instrument, the one that contributes most to miniaturization and that makes frequency agility possible is the use of one acousto-optical tunable filter (AOTF) instead of a conventional scanning monochromator or stepped-filter-wheel monochromator to obtain the required frequency (wavelength) selectivity and tunability. A typical conventional scanning monochromator has dimensions of about 15 by 15 by 10 in. (38 by 38 by 25 cm), is delicate, includes stepping motors and other moving parts, has low optical throughput, and is constrained to scan sequentially, with attendant slow switching between wavelengths. A stepped-filter-wheel monochromator is limited to the few fixed wavelengths of the filters in the wheel.

In contrast, AOTFs are rugged, monolithic solid-state units that contain no moving parts; are electronically tunable with rapid, random-access switching to any wavelength in range; offer high optical throughput; and are very small (typically, 1 $in.^3$ (16 cm^3)). Unlike monochromators, AOTFs are capable of spectrally resolved imaging. The present instrument exploits this capability to achieve microscopic imaging. Thus, the instrument can be used, for example, to measure fluorescence in single live cells, rather than being limited to measurements in bulk cell suspensions.

The figure shows the major parts of the instrument. The cell-culture-and-imaging module includes a sample carousel that contains 40 0.2-mL culture chambers. The contents of each chamber can be observed via a coverslip on the bottom of the carousel, and access to each chamber can be gained via two septa at the top. Fluids can be pumped from any of 6 reservoirs into any of the 40 culture chambers. A subsystem that maintains optimum cell-culture conditions is included in the module.

The microspectrofluorimeter is configured as an AOTF-based fluorescence microscope. The source of light is a xenon arc lamp. Images are detected by an intensified charge-coupled-device (CCD) camera. Also included in the instrument are (1) a module that contains power-supply circuits plus other electronic circuits for operating the cell-culture-and-imaging module and (2) a control module that contains the equivalent of a 486-level personal computer, with image-processing and communication circuit boards. Software in the control module controls all functions necessary for complete automation of cell culture and image-data-acquisition functions.

This work was done by Salvador M. Fernandez, Ernest F. Guignon, Ralph Levy, Sean Cobane, and Robert Kersten of Ciencia, Inc., for Kennedy Space Center. Further information is contained in a TSP [see page 1].

In accordance with Public Law 96-517, the contractor has elected to retain title to this invention. Inquiries concerning rights for its commercial use should be addressed to

Salvador M. Fernandez, President
Ciencia, Inc.
111 Roberts Street, Suite C
East Hartford, CT 06108

Refer to KSC-11835, volume and number of this NASA Tech Briefs issue, and the page number.

Microwave Treatment of Cardiac Arrhythmias

A catheter contains a coaxial cable that delivers microwave energy via a small antenna.

Lyndon B. Johnson Space Center, Houston, Texas

An experimental method of treating tachycardia involves the microwave-induced ablation of a 10-mm layer of arrhythmogenic muscle tissue at the affected inner surface of the heart. In this method, the affected tissue is heated by microwave energy applied via a catheter. A thin coaxial cable in the catheter delivers the microwave energy to the tip of the catheter. A small antenna at the tip is designed for optimal coupling of the microwave energy from the coaxial cable into the tissue. The absorption of microwave energy in the tissue causes heating, which, in turn, produces the desired lesion.

The microwave frequency must be chosen so that the microwave energy is absorbed predominantly in a surface layer of the desired thickness: if the frequency is too low, the microwaves propagate too far through the tissue, producing heating that is too diffuse; if the frequency is too high, the energy is dissipated in too thin a layer near the surface. The optimum frequency is expected to lie in the range of 4 to 6 GHz, the exact value depending on the electrical conductivities and permittivities of blood and heart muscle (see Figure 1).

In comparison with other methods that involve direct-current pulses or radio frequencies below 1 GHz, this method may prove more effective in treating ventricular tachycardia. This is because the present method provides for greater control of the location, cross-sectional area, and depth of a lesion via selection of the location and design of the antenna and the choice of microwave power and frequency. An apparatus has been constructed to test the concept in experiments on microwave heating of simulated heart tissue (see Figure 2).

This work was done by G. D. Arndt of Johnson Space Center; J. R. Carl, G. W. Raffoul, and V. G. Karasack of Lockheed Engineering and Sciences Co.; and T. Pacilio and C. F. Piper of Baylor College of Medicine. Further information is contained in a TSP [see page 1].

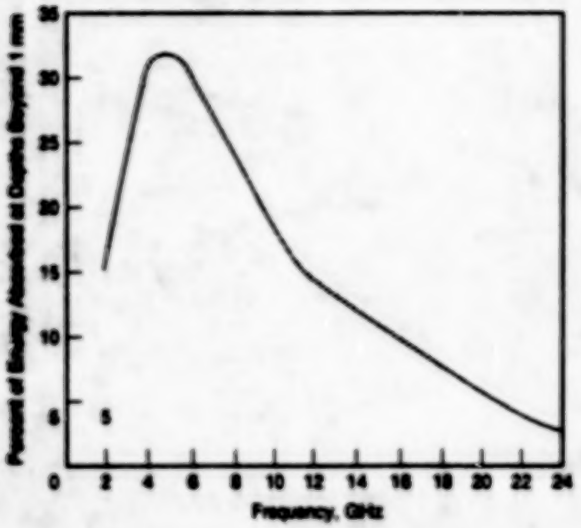

Figure 1. Heating Effects of Microwaves in heart tissue were mathematically modeled, using assumed values of the permittivities and electrical conductivities of heart muscle and blood.

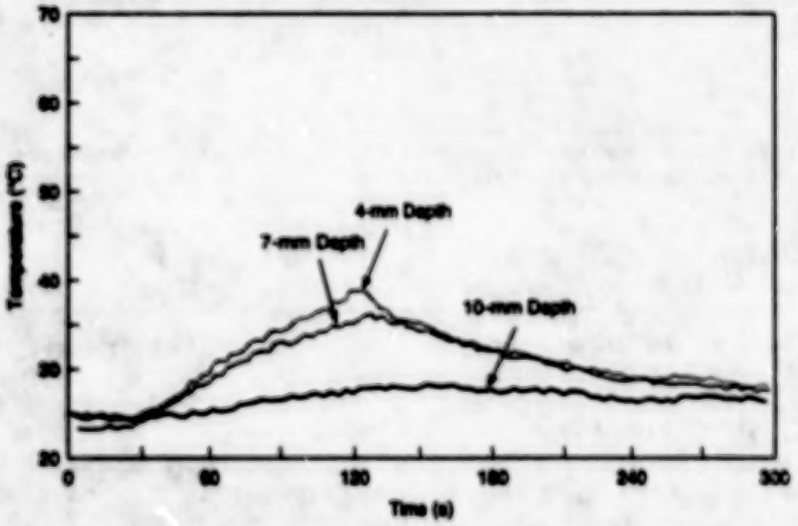

Figure 2. Temperature Ramping is shown here as a function of 4.10-W microwave exposure for various depths.

This invention is owned by NASA, and a patent application has been filed. Inquiries concerning nonexclusive or exclusive license for its commercial development should be addressed to the Patent Counsel, Johnson Space Center [see page 1]. Refer to MSC-22483.

END

12-22-99